

Geophysical Research Letter

Supporting Information for

Unveiling the Global Extent of Land Subsidence: The sinking crisis

Tsimur Davyzenka¹, Pejman Tahmasebi^{1*}, Nima Shokri²

¹Colorado School of Mines, Golden, CO 80401, USA

²Institute of Geo-Hydroinformatics, Hamburg University of Technology, Am Schwarzenberg-Campus 3 (E), 21073 Hamburg, Germany

*Corresponding author: Pejman Tahmasebi (tahmasebi@mines.edu)

Contents of this file

Text S1 to S3

Figures S1 to S16

Tables S1 to S6

Captions for Data Files S1 to S3

Datasets S1 to S3 are available at:

<https://doi.org/10.5281/zenodo.10223636>

Text S1

1. Preparation of Global Subsidence Dataset.

The compilation of the subsidence dataset (253,882 data points) was conducted using 221 individual publications/open-source data on land subsidence. The top 34 sources in terms of extent of subsidizing area were added to the dataset, capturing the entirety of the study area (thousands of subsidence points per record), and the rest 193 studies constituted only single point per subsidence incident. In addition, we included 19221 data points from a compilation of global GPS stations. In cases where GIS files were not available, maps provided by the publication were digitized (Rohatgi, n.d.) and subsidence locations with their respective rates were extracted. The format of these maps included ones with full continuous mapping of subsidence, contour maps, and individual subsidence points. An example of the process is provided in Supplementary Figs. 1 & 2. Here, the first figure shows reported land subsidence rates in Mexico City, Mexico (Auvinet, Méndez, & Juárez, 2017), and the second figure shows how the digitized points look in the final global dataset (Supplementary Fig. 2, A). The raw digitized points (Supplementary Fig. 2, B) were then resampled to match the 30" resolution of input maps. This means, that all points that were at sub-30" resolution were averaged and only one value was assigned for each 30" tile. We ensured that the point density is larger than 1 point per 30", and not smaller so that sub-30" points would be averaged. In cases where any subsidence data point was too far to the closest pixel, for which there is corresponding feature data available, those points were disregarded (at >0.02 degrees threshold). Once all subsidence points were compiled into a single dataset, the total number of data was 253,882. After these points were resampled to one point per 30" tile with and aforementioned points were disregarded, the total number of data was reduced to 164,929.

To be later used for training, from the compiled dataset we selected only subsidence rates at >0mm/year cutoff, in the interest of removing negative non-subsiding locations. Additionally, each local study was declustered by randomly removing 75% of points in each record, in order to reduce the weight of any individual subsidence site on the final prediction. As a consequence, this resulted in 46,154 total subsidence points. Next, to provide the network with no-subsidence scenarios, an approach that is generally followed consists of populating the dataset with values that represent non-subsidence or 0-subsidence rate. These points are randomly selected either from the rest of the map or from known non-subsidence locations in 1-1 ratio to the non-0 values (Arabameri et al., 2022; Ebrahimi, Feizizadeh, Salmani, & Azadi, 2020; Wen et al., 2022). To accomplish that and to identify non-subsidence areas, we use a recent major study on global subsidence susceptibility (Herrera-García et al., 2021) and randomly select data from very-low subsidence susceptibility areas. In order to reduce the effect of 0-subsidence points and avoid artificial boosting of model performance metrics (such as R^2 score), we further reduced the number of non-0 points to constitute the ratio of 2 – 1 (instead of 1-1). The final number of selected 0-subsidence points amounted to 23076 (1/2 the number of non-0 values).

2. Selection of Input Variables.

A total of 23 spatially continuous predictor variables were used in this study to train the model. The maps for the variables are provided at different resolutions, but all of them were eventually resampled to 30" resolution and cropped to 180W-180E-56S-90N extent. The maps represent global coverage of climatic, topographic, geologic, soil, and other subsidence proxies. The variables are assembled and summarized in Supplementary Table 2 with relevant information regarding pre-processing, source, extent, and resolution.

The compilation of the predictor maps that are believed to be proxies of subsidence began with a review of studies that attempted to predict and map subsidence susceptibility or the rate at a local scale (22–25, 48–50, 84–92). The number of input features in these studies was around 10 to 15 and allowed for achieving reasonable accuracy. However, as predicting subsidence rates at a global scale involves much more complexity, the number of input features in our case had to be larger to fully capture the underlying conditions of a given location.

In general, studies that attempted to predict subsidence (either susceptibility or in very few cases rates), used the following predictors as inputs for their models: land use and land cover, lithology, distance to roads, distance to faults, distance to rivers, climate, precipitation, sediment thickness, groundwater (GW) extraction proxies, slope, topographic wetness Index, aspect, terrain roughness index, plan and profile curvature, vegetation (EVI2, NDVI), elevation, stream power index. With these variables in mind, we compiled our input set of 23 inventory maps, focusing on proxies for groundwater withdrawal and aquifer depletion, since it is believed to have a major effect on subsidence. This set of variables is an attempt to provide the network with sufficient information about the aquifer balance, where one set of predictors is responsible for aquifer depletion, and another is for aquifer recharge.

As such, variables that answer the question or provide a reasonable proxy of how much water leaves the aquifer are: GW abstraction, population, evapotranspiration, temperature (and all temperature related variables). Then, variables that are proxies for the degree to which the aquifer is recharged are: GW Recharge and precipitation (and all other precipitation variables). Next, as the magnitude of land subsidence invariably depends on the total thickness of the aquifer or sediments (Smith & Majumdar, 2020), (the higher the thickness, the greater potential subsidence is), we selected the following parameters: water storage thickness, soil and unconsolidated sediment thickness, GW storage capacity.

Once the variables for groundwater/aquifer balance were compiled, the rest of the input vector was complemented by variables related to climate, geology, soil properties, topography, etc.

3. Calculating Zonal Statistics

Once the model was trained and global subsidence map produced, we calculated relevant zonal statistics for different regions and land types, defined by the following boundaries: administrative boundaries (such as countries), regions, biomes, anthropogenic

biomes, lithology, land cover, and climate (Table S4). Out of all these zones, only land cover and lithology were used for training. For each class of any zone, we calculate the following statistics: mean and maximum subsidence rate (based on >1mm/year subsidence rate cutoff), the cumulative extent of land subsidence, and potentially affected population (based on >5, 15, 25, 50 mm/year cutoffs). In addition, we calculated the corresponding percentages of the zone's total area (zones total land area in cases of administrative boundaries and regions) and total population. For administrative boundaries, we also calculated the extent of total urban and dense settlement areas (UDS) that are affected by subsidence (based on the same thresholds). A part of zonal statistics for administrative boundaries and regions is provided in Tables S5 and S6, and full statistics are compiled in the second supplementary spreadsheet.

Text S2

To evaluate the contribution of each variable toward final model performance, we applied a state of the art framework in machine learning (ML) interpretability - SHAP (SHapley Additive exPlanations), (Lundberg & Lee, 2017). Based on cooperative game theory, the SHAP method is a way to reverse-engineer the results of any complex predictive algorithm and follow the decisions made by the model. This approach allows analyzing importance of individual features, as well as detecting if a feature has a positive or negative impact on the output. To calculate a single importance score for each feature, we calculated SHAP values for all 62306 samples in the training set (1000 of which are randomly selected and are used as reference to provide a baseline for relative feature importance) and calculated the mean absolute score. The scores for every feature in the dataset are provided in Table S3, next to other relevant feature statistics. The variables are listed in the descending order of their importance. Land Cover and Lithology were not included in the analysis, since SHAP library does not currently provide a consistent and reliable method for evaluating feature importance of one-hot encoded features.

Next, the SHAP framework allows us to analyze the feature's impact with the use of summary plots (Figure S7). The figure includes all continuous features, sorted by their average absolute importance. Each feature on the figure has a set of points associated with it, that are scattered either to the left or to the right side of the 0-line. The 0-line represents the mean output of the model, and a point's location to the right indicates that for that single prediction (e.g., the model predicted that subsidence rate equals 100 mm/y in a certain location), the feature's presence in the dataset leads the model to produce prediction, that is larger than the mean prediction value. And, if the point is located to the left of the 0-line, then for that single prediction (again, only one of the total 62306 subsidence points in the training set), the presence of that feature resulted in a predicted subsidence rate that is smaller than an average model prediction. The next important piece of information that each point contains is the magnitude of that feature value, compared to all values of that feature within the dataset, which is encoded in its color. This means that by analyzing the location of the points and their colors, we can observe whether a)

smaller values of the feature lead to an increase in land subsidence, b) larger values lead to larger subsidence, or c) a mixed relationship, meaning that under certain conditions higher values of that feature will lead to increase in subsidence, but under different conditions, the relationship will be inverted. This functionality has allowed for comprehensive feature analysis, which is included in Section 3.2 of the main manuscript.

Text S3

Areas that are predicted to have significant subsidence rates ($> 5 \text{ mm/y}$) can be found on all continents (Figure 2 and Figures S8-14), with most located in South, Southeast, Central, and East Asia (77.7%), as well as South and Central America (11.2%) regions. Documented areas of land subsidence are well captured by the prediction map, including areas for which only a single subsidence point was used during model training. These areas include San Joaquin Valley, Las Vegas Valley, New Orleans, Houston (USA); North China, Fenwei, and Yangtze River Deltaic plains (China); Tehran, Rafsanjan, and Zarand-Kerman plains (Iran); Sumatra and Java islands (Indonesia); Nile delta (Egypt); Mekong delta (Vietnam); Gandhinagar and Kolkata (India). Extensive areas with high rates that have not been documented to date include Indo-Gangetic plain (India); Mississippi alluvial plain, major areas in west Columbia, Ecuador, Panama, Uzbekistan, Turkmenistan, south-east Afghanistan, and north-west Pakistan.

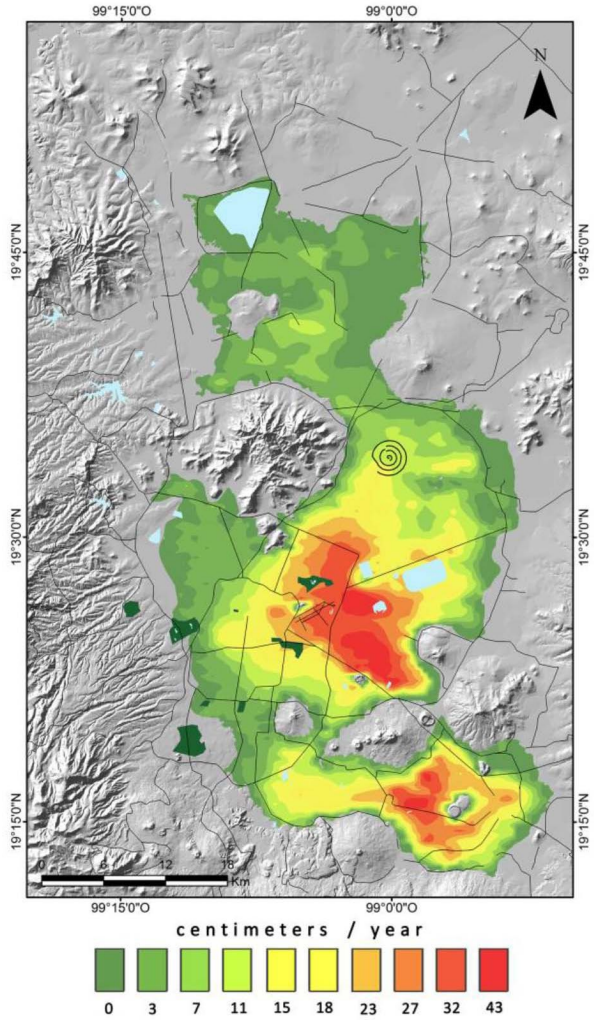


Figure S1. Digitization example. Demonstration of One of the reported subsidence maps, that was digitized (converted to longitude/latitude/rate format) and used to compile the global subsidence dataset.

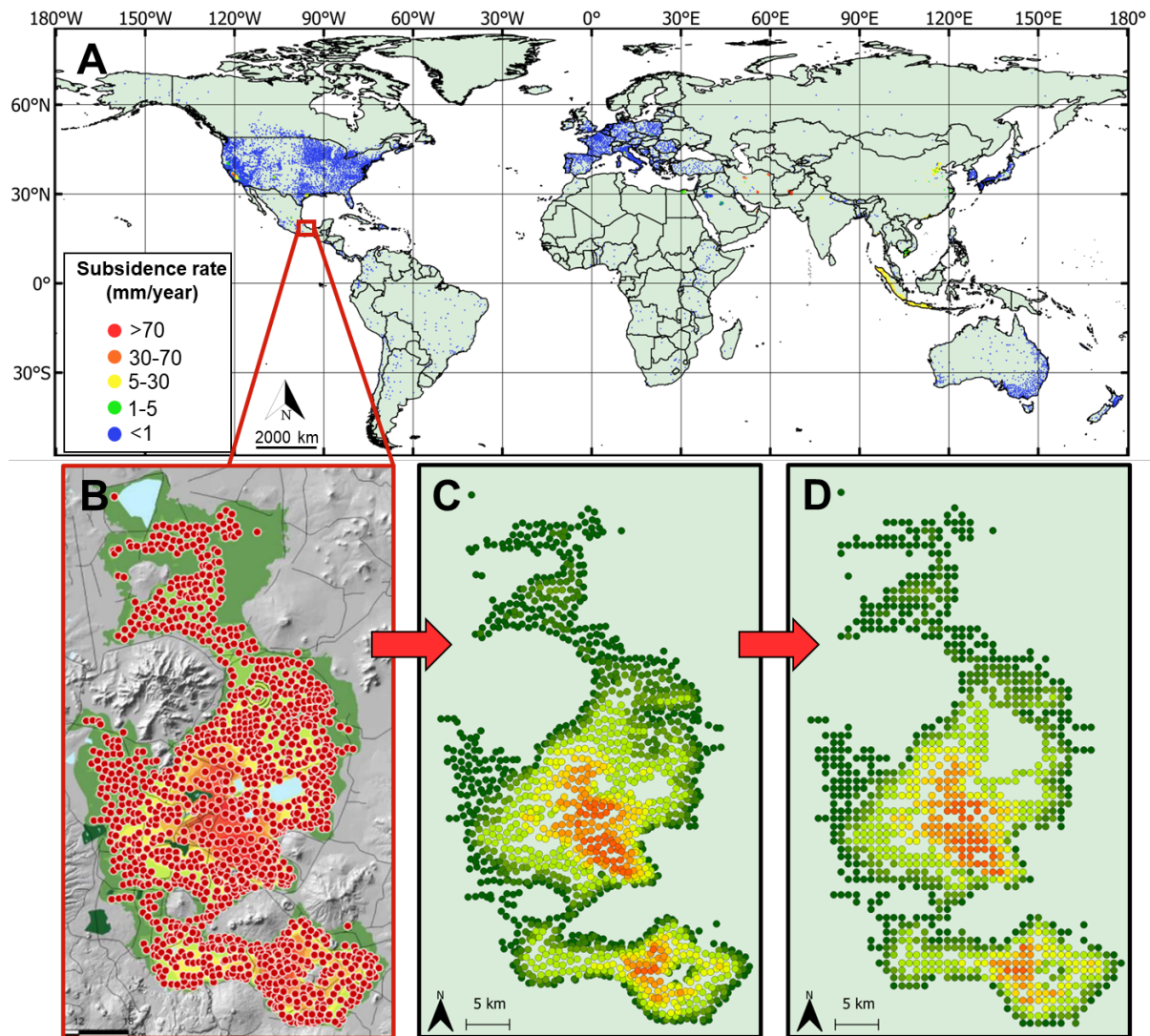


Figure S2. Digitization workflow. Spatial distribution of compiled global subsidence records (a), points detected by the digitization algorithm, based on the provided colors in the legend of the original image in figure S1 (b). Visualization of the extracted points in GIS software, based on extracted longitude, latitude, and rates (c). Final locations of the points, after resampling and snapping on the 30" tiles of the input maps (d).

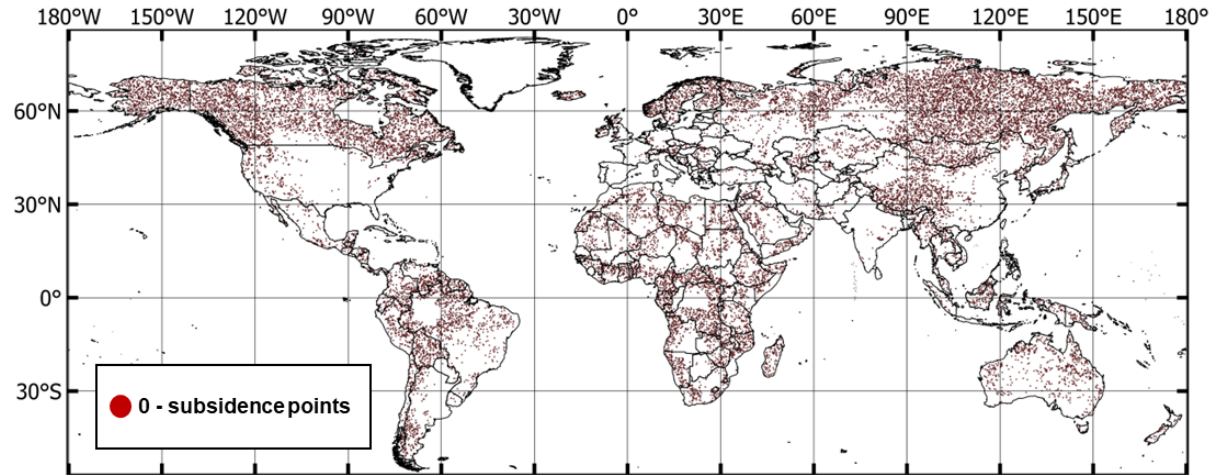


Figure S3. Randomly selected locations of the zero-subsidence points. The data was randomly selected from very-low subsidence susceptibility areas provided by Herrera-García et al., 2021, in the corresponding resulting ratio or 49/35/16.

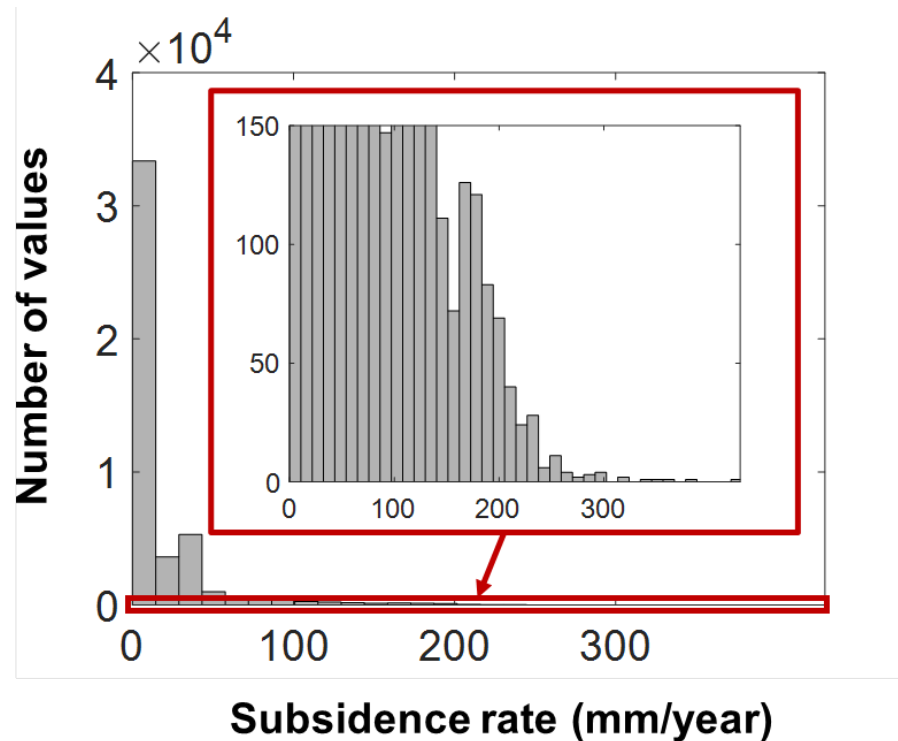
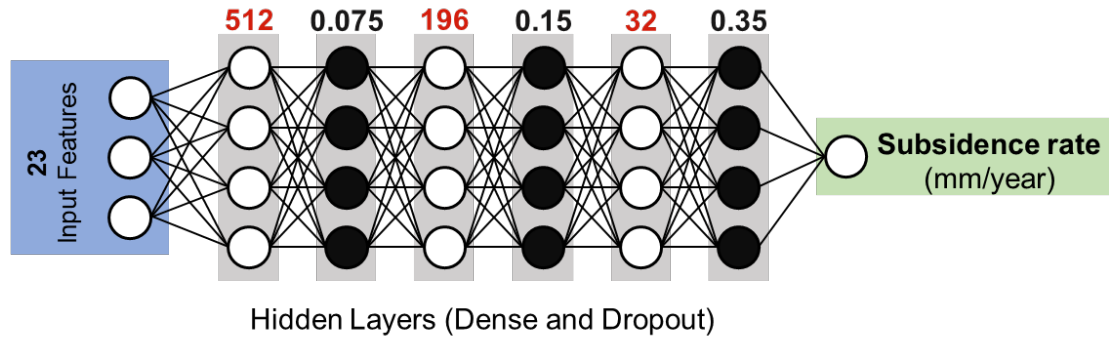


Figure S4. Frequency distribution of the subsidence values.



Parameter	Value	Parameter	Value
Number of hidden layers	3	Model optimizer	Adam
Number of neurons	512-196-32	Learning rate	0.001
Number of epochs	960	β_1	0.9
Training/Validation/Test	81/9/10 %	β_2	0.999
Batch size	1,024	ε	1×10^{-7}
Training + Validation data size	62,306	Framework	Keras (Python)

Loss function: **MSE**

Activation functions: **ELU**

Figure S5. Model architecture and specifications used in this study.

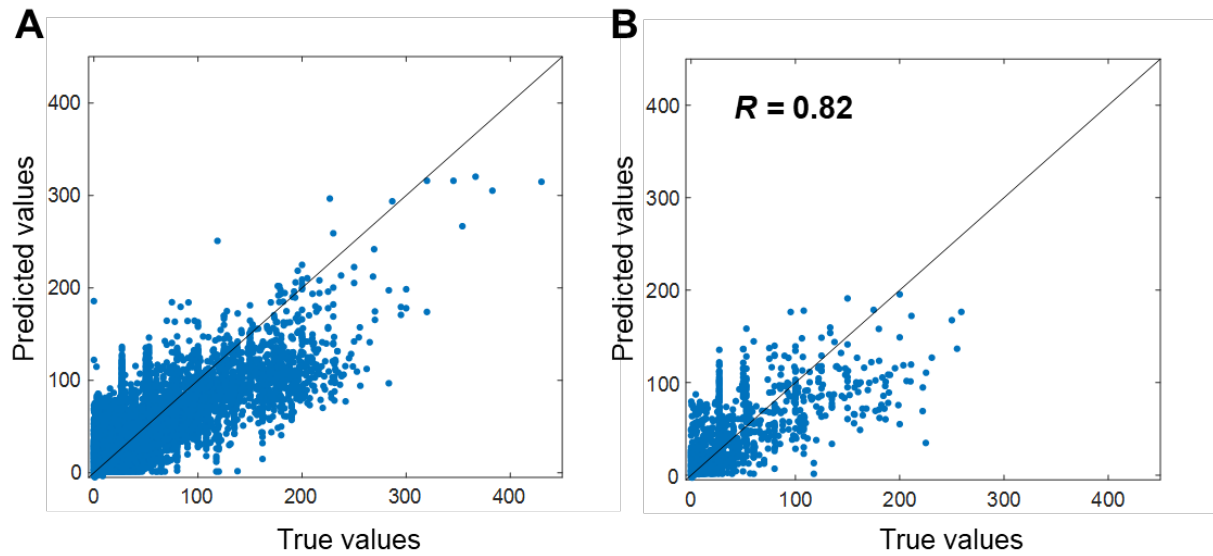


Figure S6. Parity plots between predicted and exact values. (A to B) Training and validation sets (a). Test set (b).

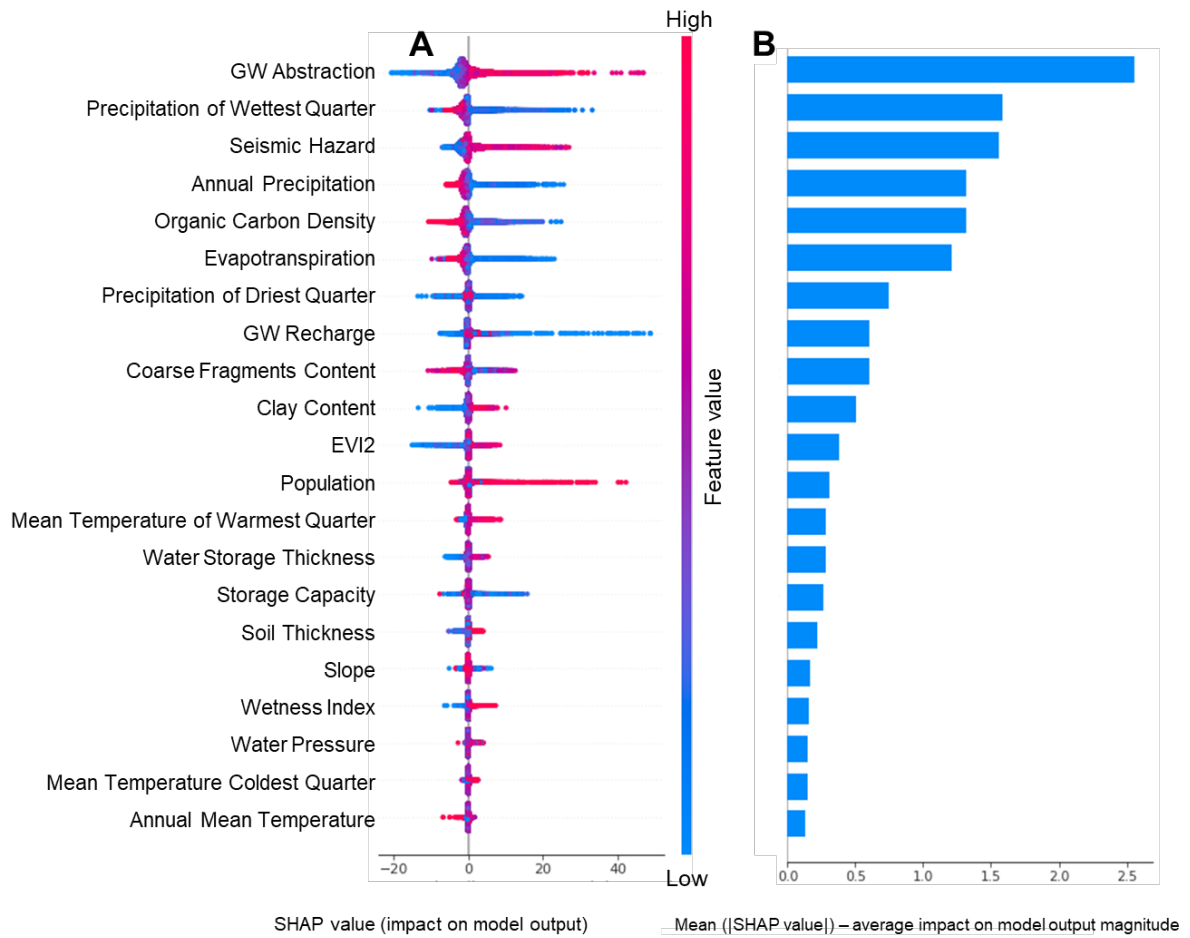


Figure S7. Feature importance of the 60 predictors. Demonstration of the direct/inverse/mixed relationship between the predictors and subsidence rates (a), overall feature importance (b).

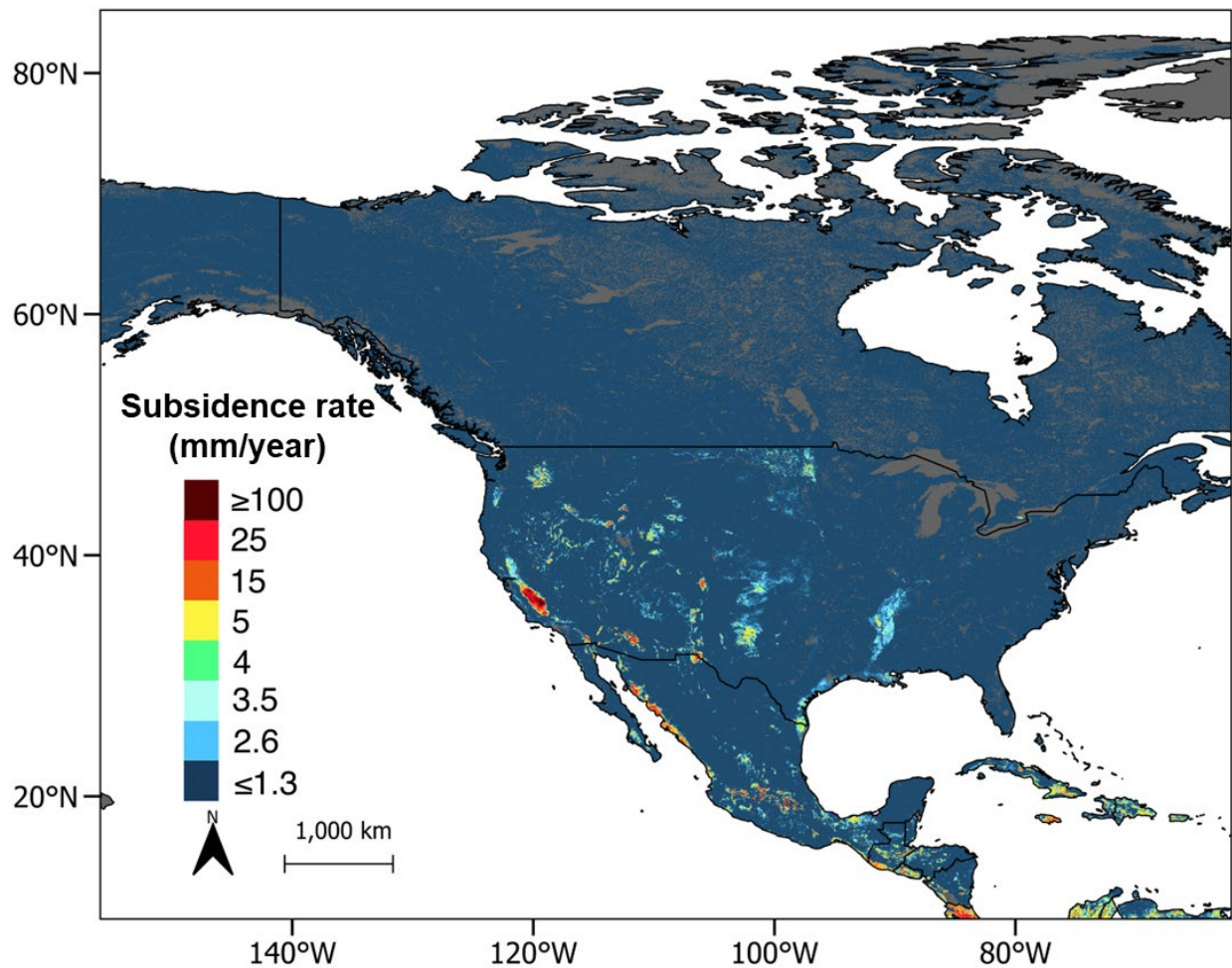


Figure S8. Subsidence rates prediction map for North and Central America and the Caribbean.

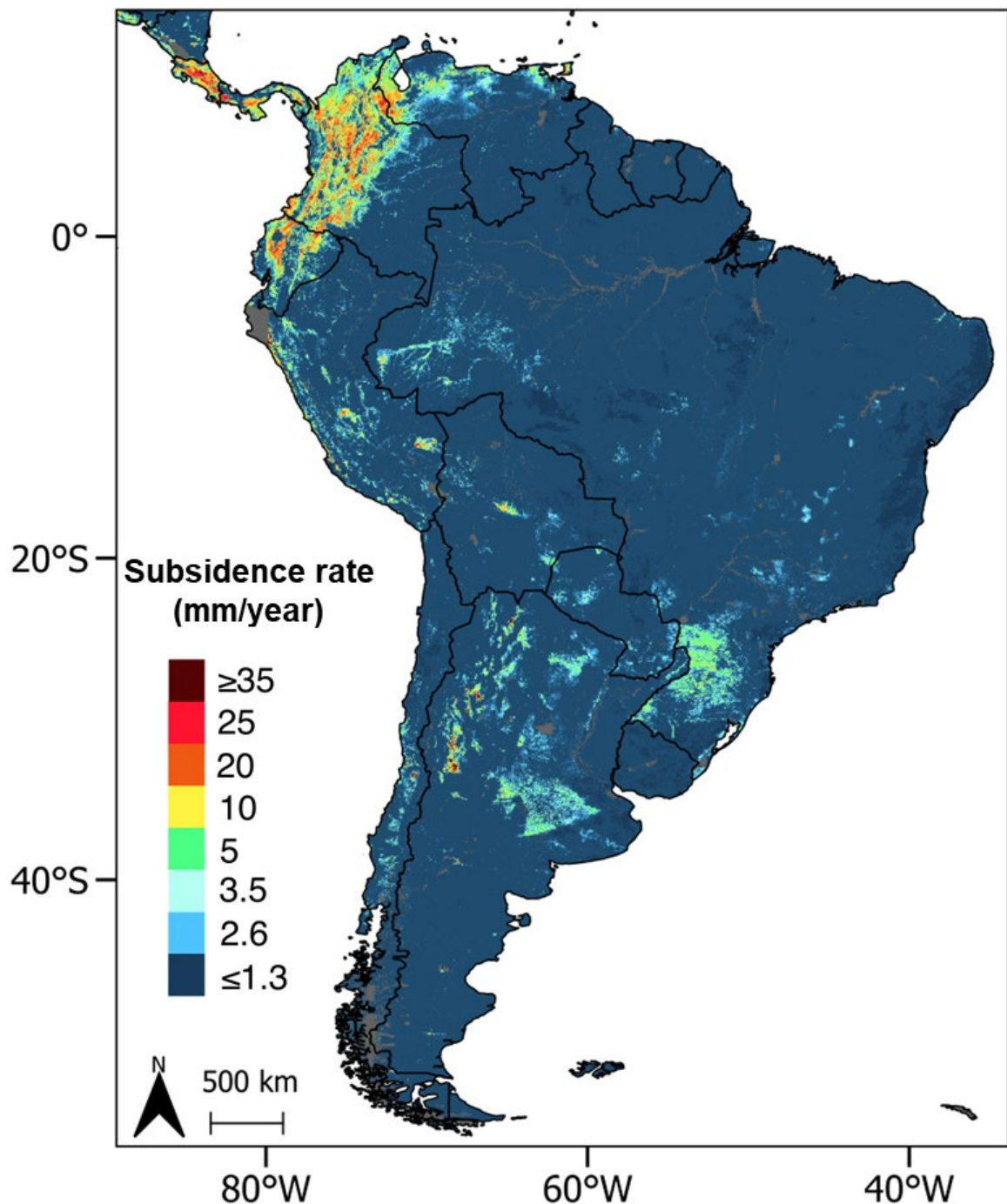


Figure S9. Subsidence rates prediction map for South America.

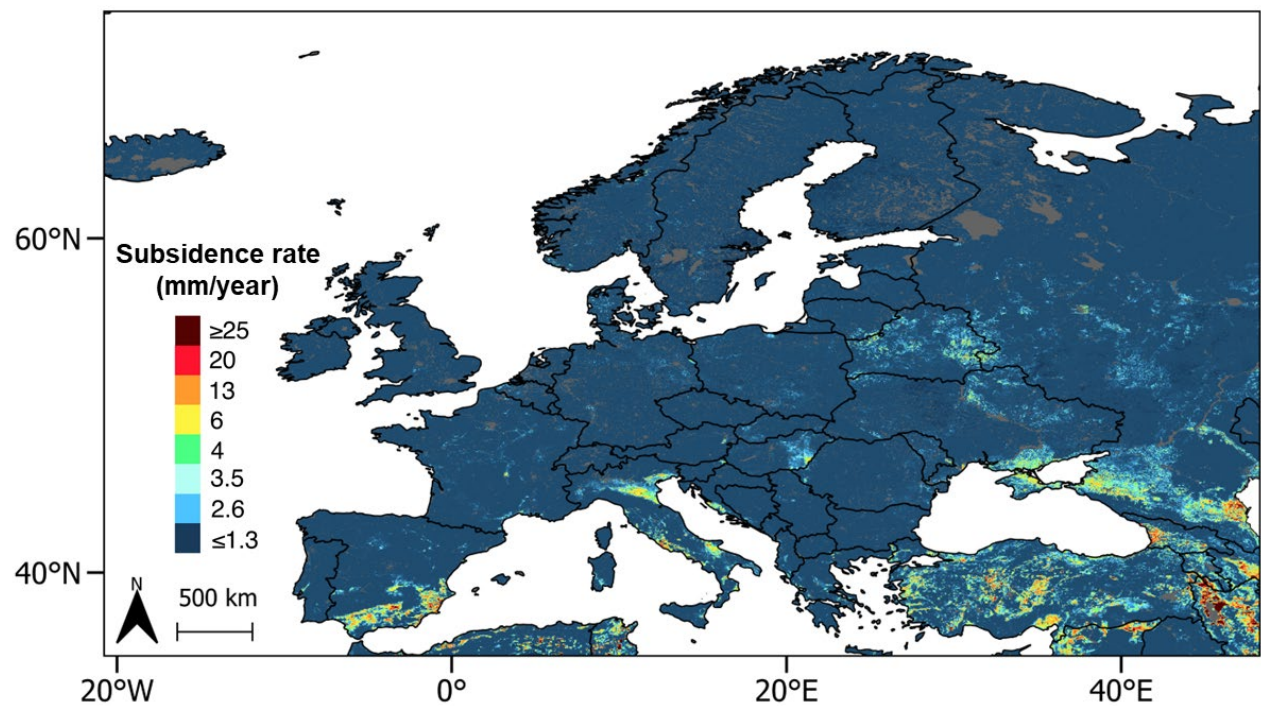


Figure S10. Subsidence rates prediction map for Europe

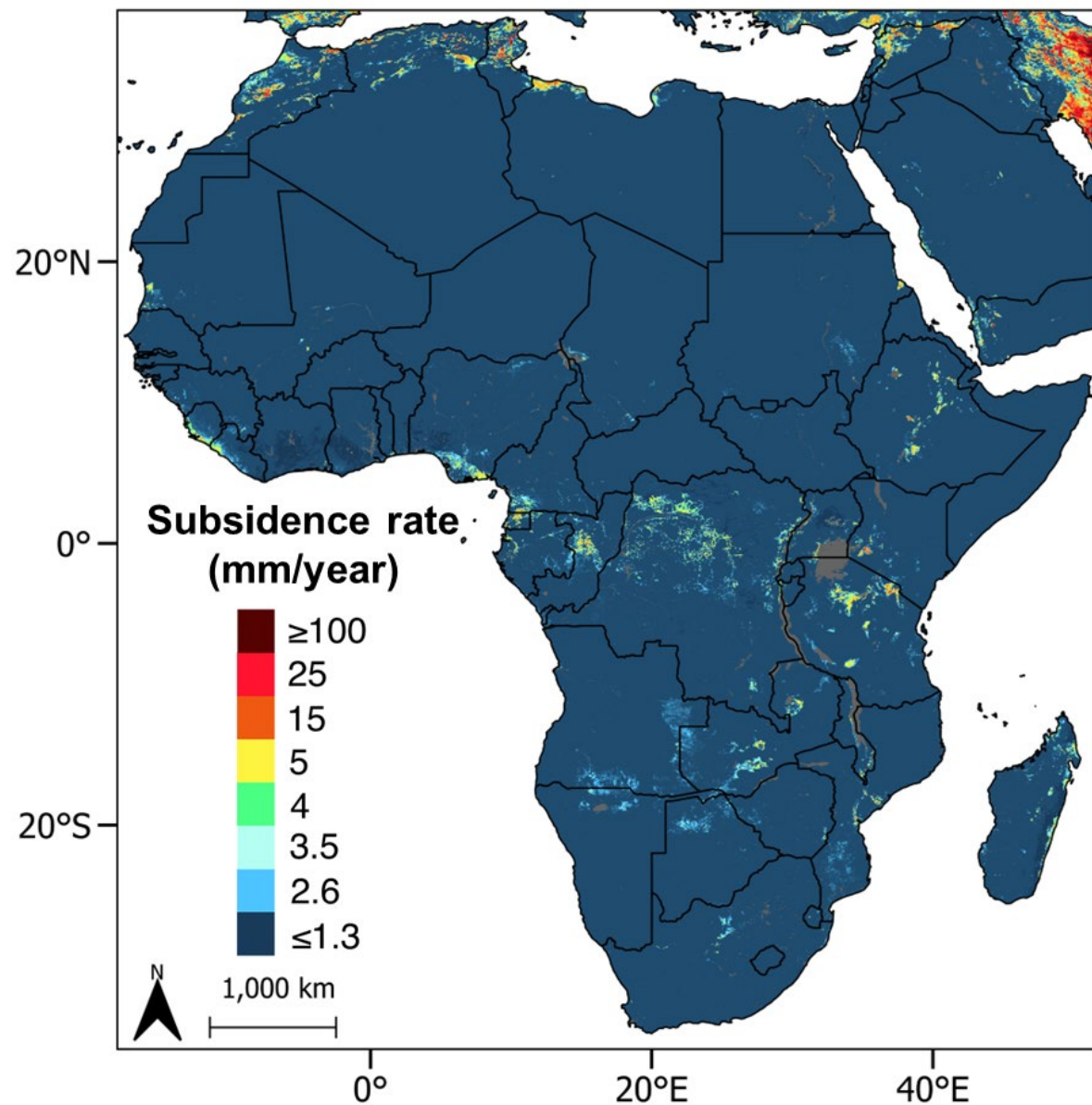


Figure S11. Subsidence rates prediction map for Africa and the Arabian Peninsula.

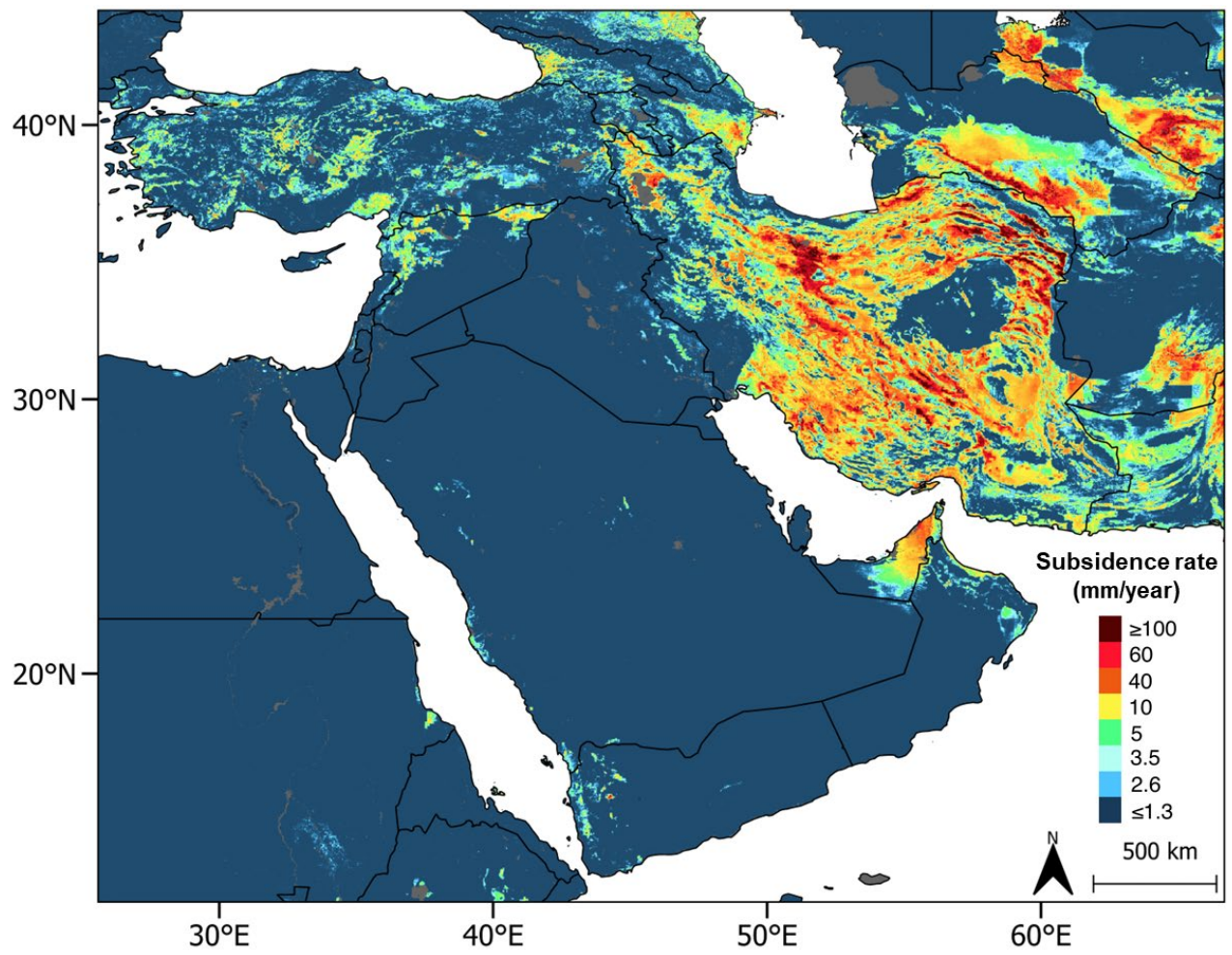


Figure S12. Subsidence rates prediction map for Middle East.

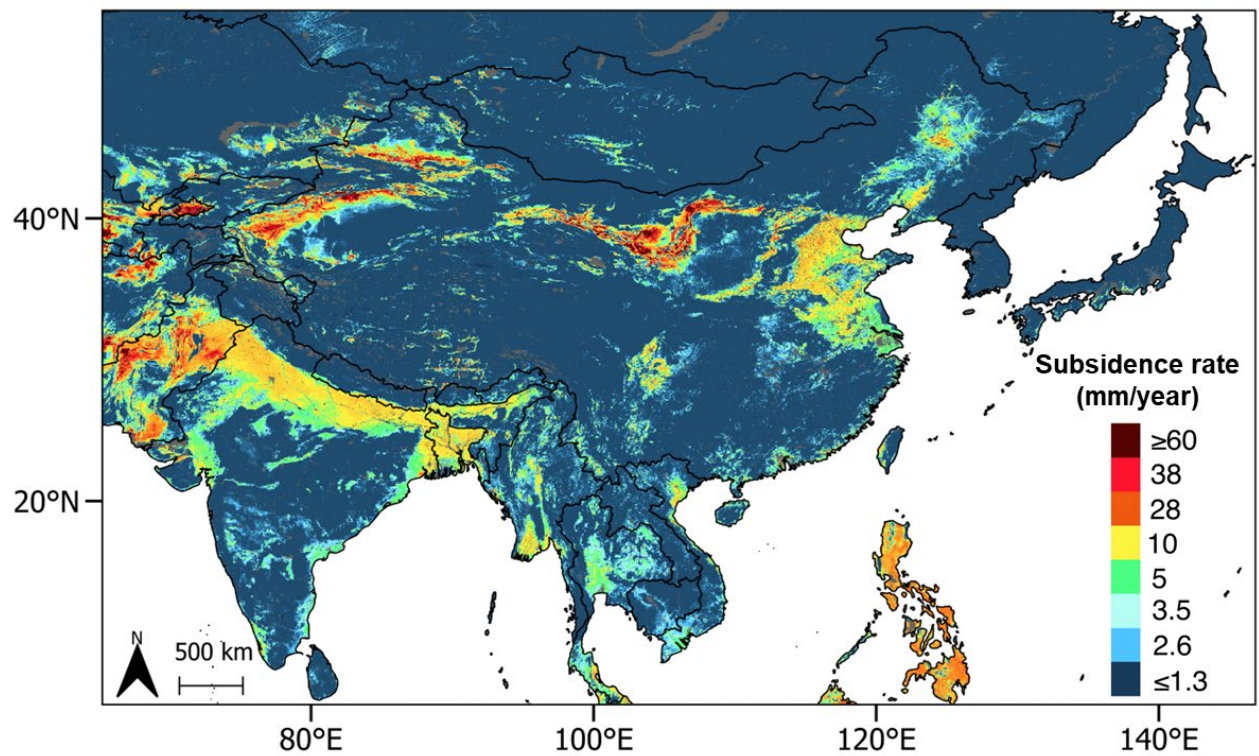


Figure S13. Subsidence rates prediction map for Central, South, and East Asia.

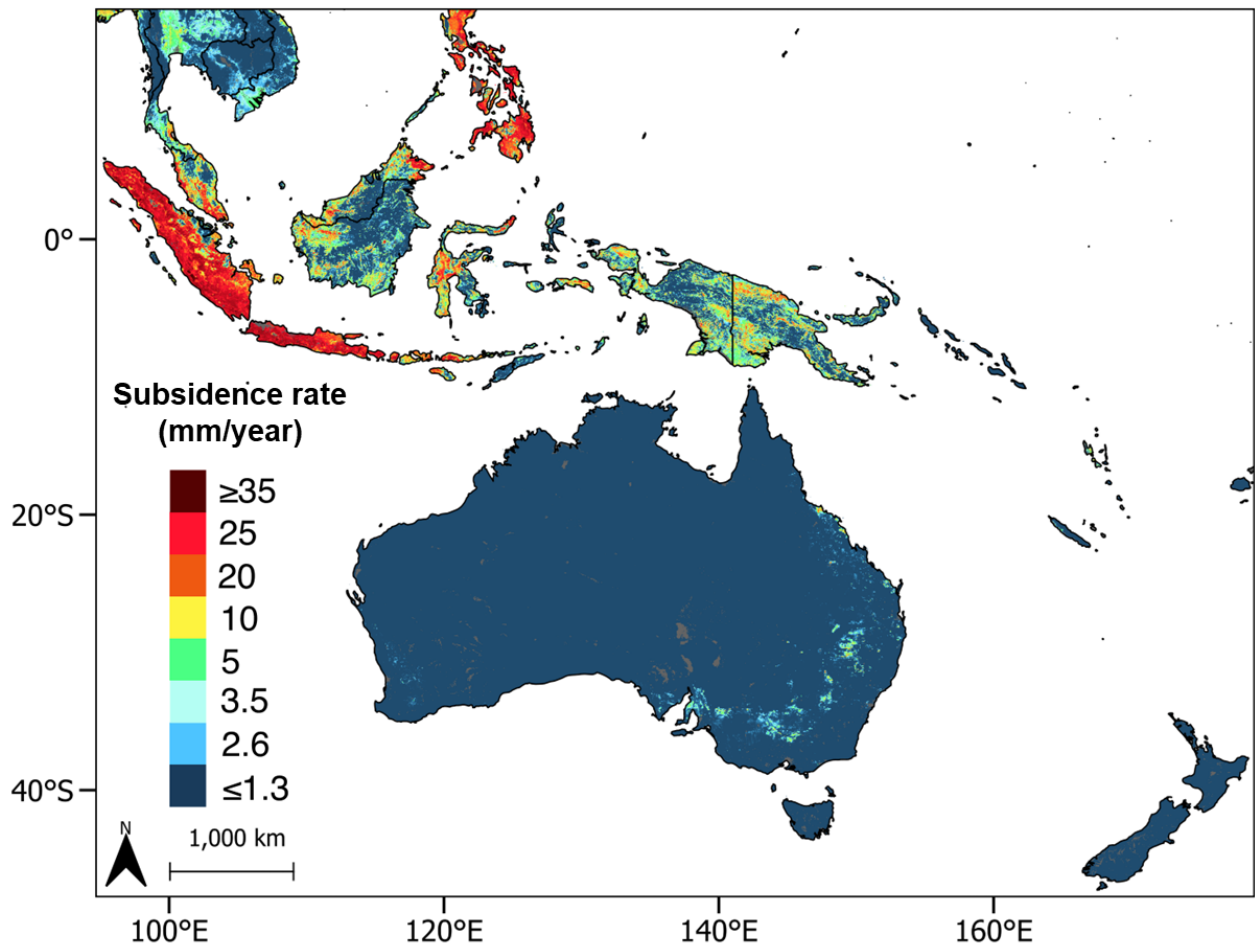


Figure S14. Subsidence rates prediction map for South-East Asia, Oceania, and Melanesia.

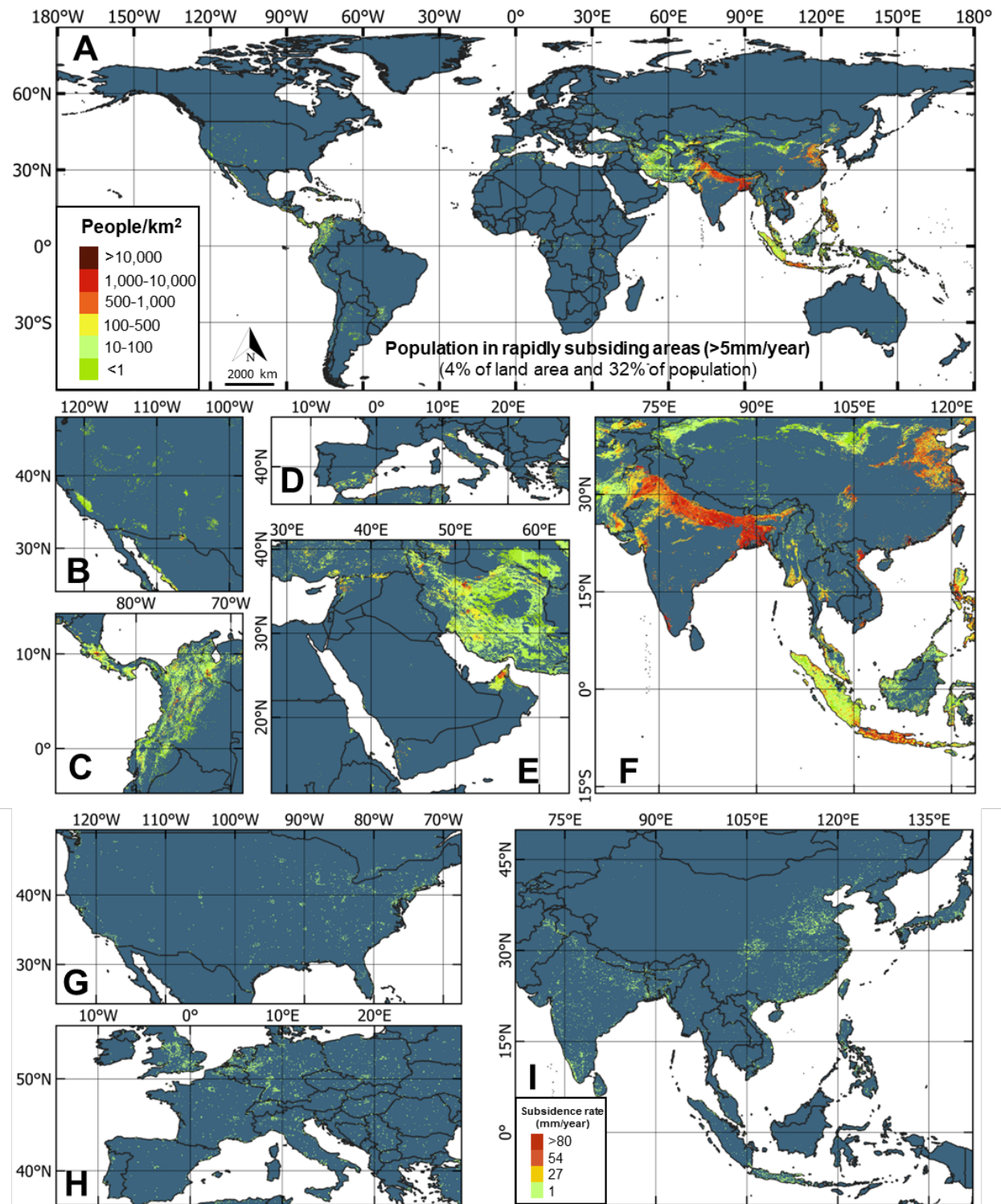


Figure S15. Affected population and infrastructure. Population in areas where subsidence rates exceed 5 mm/year (a), zoomed in areas of interest (b) to (f). Subsidence in urban and dense settlement areas (g) to (i).

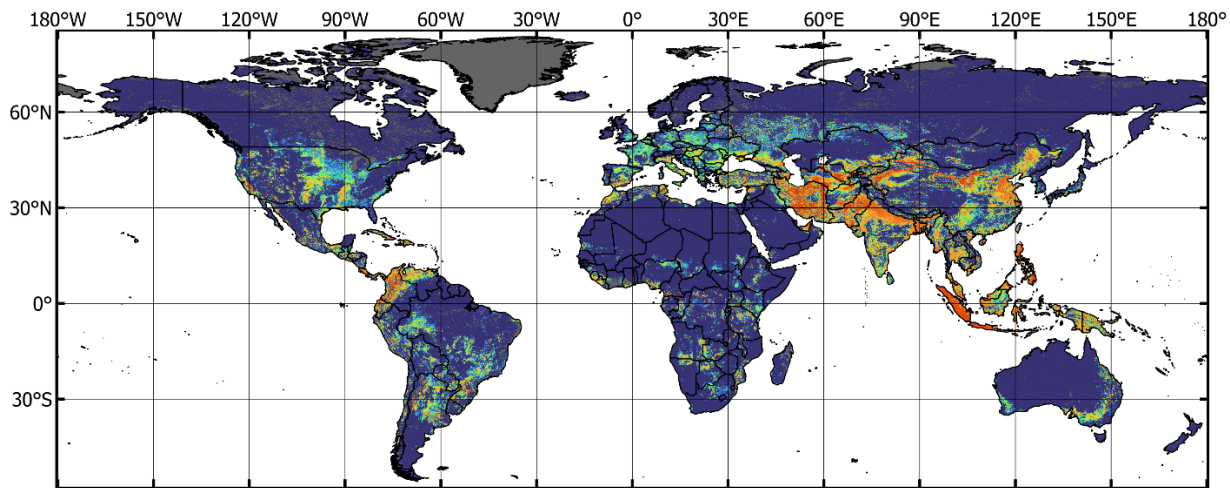


Figure S16. Uniform distribution applied to the subsidence rates to enhance the visualization.

	Location/Source	Number of Extracted Points per source.	Subsidence rate range (mm/y)	Number of points, after averaging overlapping studies. Subpixel points were averaged and assigned to a single pixel. Points that are too far (>0.02 degrees) from the closest pixel with data were disregarded.	Number of points (after declustering) used for training + validation + testing (only >0mm/y values were used).
1	Central Valley, CA, USA TRE Altamira ('TRE Altamira Dataset', 2015)	101,135	0.00008-265	76419	19105
2	Indonesia (Chaussard, Amelung, & Abidin, 2012) - overlaps with 11	19487	30-120	17912 *shared with (11)	4419*shared with (11)
3	Mekong Delta, Vietnam (Erban, Gorelick, & Zebker, 2014)	14444	5-40	9692	2423
4	San Joaquin Valley, CA, USA ('Subsidence in San Joaquin Valley', n.d.)	12,297	27-222	10699	2675
5	Albuquerque, NM, USA (Heywood, Galloway, & Stork, 2002)	2148+2499 +3134+1429=9210	0.65-117.6	3156	789
6	Rafsanjan, Iran (Motagh et al., 2017)	3656+5402=9058	50-300	1079	270

7	Beijing, China (M. Chen et al., 2016)	8,064	0.05-95	3458	865
8	Lisbon, Portugal (Heleno et al., 2011)	2770+3095=5865	1.05-9.2	784	196
9	Central and Northern Arabia (Othman et al., 2018)	4,971	1-12	4924	1231
10	Shanghai, China (Dong, Samsonov, Yin, Ye, & Cao, 2014)	4939	0-30	2296	490
11	Jakarta, Indonesia (Ng et al., 2012)	4130	0-162.5	see (2)	see (2)
12	Hampton Roads, VA, USA (Bekaert, Hamlington, Buzzanga, & Jones, 2017)	3,466	0.00003 – 9.3	1772	443
13	Hebei Plain, China (X. Li et al., 2021)	3338	10-60	3260	815
14	Ho Chi Minh City, Vietnam (Ho Tong Minh, Van Trung, & Le Toan, 2015)	3252	5-25	239	60
15	Anthemountas, Greece (F. Raspini, Loupasakis, Rozos, & Moretti, 2013)	3136	0.75-32.5	283	71
16	Guangdong, China (Du et al., 2020)	3066	10-35	1048	262
17	Tehran, Iran (Haghshenas Haghghi & Motagh, 2019)	2499	50-200	1277	319
18	Saudi Arabia, (Othman & Abotalib, 2019)	2,259	1-10	1887	472
19	Remah, UAE (El Kamali et al., 2021)	2004	25-40	393	98
20	Firenze–Prato–Pistoia Plain, Italy (Del Soldato, Farolfi, Rosi, Raspini, & Casagli, 2018)	1832	0-25	1131	83
21	Chiayi, Taiwan (Hung et al., 2018) - overlaps with (33)	1795	1-5	1279 *shared with (33)	320 *shared with (33)
22	Mashhad Plain, Iran (Salehi Moteahd, Hafezi Moghaddas, Lashkaripour, & Dehghani, 2019) - overlaps with (32)	579+905=1484	100-300	677 *shared with (32)	169 *shared with (32)
23	Mexico City, Mexico (Auvinet et al., 2017)	1,481	30-430	403	101
24	Mexico City, Mexico (Cigna & Tapete, 2021)	1407	50-400	231	58
25	Quetta, Pakistan (Kakar, Kakar, & Barrech, 2020)	1338	40-100	1270	318
26	Perth Basin, Australia (Parker, Filmer, & Featherstone, 2017)	1203	0-30	387	45
27	Houston, USA (Yu, Wang, Kearns, & Yang, 2014)	1198	4-22	1014	254
28	Gioia Tauro, Italy (Federico Raspini, Cigna, & Moretti, 2012)	1,146	2.15-17.15	479	120
29	Yangon, Myanmar (van der Horst, Rutten, van de Giesen, & Hanssen, 2018)	1076	10-40	169	42
30	Nile Delta, Egypt (Gebremichael et al., 2018)	1039	3-9	1022	256
31	New Delhi, India (Malik, Kumar, Perissin, & Pradhan, 2022)	818	10-30	315	79
32	Mashhad, Iran (Khorrami, Abrishami, Maghsoudi, Alizadeh, & Perissin, 2020)	616	30-190	see (22)	see (22)
33	Central Taiwan (Hwang et al., 2016)	477	10-80	see (21)	see (21)

34	Hong Kong, China (Q. Chen et al., 2010)	308	2-6	112	28
35	The rest 192 points were obtained from (Bagheri-Gavkosh et al., 2021) (includes 7 points from digitized maps), using mean reported values, and one point from (J. Li, Wang, Michel, & Russell, 2020)	193	0.01-30	144	144
36	Global dataset of GPS stations. (Blewitt, Kreemer, Hammond, & Gazeaux, 2016)	19221	-100 - 39.91	15718	9134
	TOTAL	234661	0-430	164929	46154

Note: Sources that have several values separated by “+” represent the number of figures that were digitized and points per figure that were extracted. Subsidence records of overlapping studies (one pixel of corresponding input values had more than one subsidence point) were averaged, therefore the final dataset size is **70779** points.

Table S1. Reported local land subsidence, used for the compilation of the global dataset.

Predictor	Pre-processing	Source	Projection	Extent	Resolution
Land Cover	-	GLC2000 ('Joint Research Centre, Global Land Cover 2000 (2003)', n.d.)	GCS WGS 1984	180W-180E, 56S-90N	30"
Lithology	Original vector layers were rasterized and resampled to 30" resolution.	GLiM (Hartmann & Moosdorf, 2012)	World Eckert IV	180W-180E, 90S-90N	-
Slope	Original raster layers for individual continents were merged into a single geotiff. Slope was calculated from the final Elevation layer.	GTOPO30 Digital Elevation Database (USGS, 1996)	GCS WGS 1984	180W-180E, 90S-90N	30"
Population	Population density for 2010, sustainability scenario. Resampled to match GTOPO30 using nearest neighbor.	Shared Socioeconomic Pathways (Gao, 2020)		180W-180E, 55.8S-83.6N	30"
Average soil and sedimentary-deposit thickness (m)	-	Pelletier, et al. (Pelletier et al., 2016)		180W-180E, 60S-90N	30"
Topographic Wetness Index	The original .nc file was converted to a geo-tiff raster.	Marthews, et al. (Marthews, Dadson, Lehner, Abele, & Gedney, 2015)		180W-180E, 56.35S-86.09N	30"
Groundwater Abstraction	-	Water Footprint Network (Mekonnen & Hoekstra, 2011)		180W-180E, 55.9S-83.1N	5'
Clay Content	Average maps were constructed for the maximum available depths (0-30 cm for Soil Organic Carbon Content, and 0-200	SRIC-SoilGrids - 1km version (Hengl et al., 2017)	Goode Homolosine	180W-180E, 56S-82.7N	30"
Coarse Fragments Content					

Organic Carbon Density	cm for all the rest). Original geo-tiff files were reprojected to WGS 1984, mean values per pixel were calculated using QGIS raster calculator.				
Water Vapor Pressure	Original 12 geo-tiff files, storing mean data for each corresponding month of a year, over 1970-2000's were averaged using QGIS raster calculator, to ultimately obtain a map of mean values 1970-2000's	WorldClim (Fick & Hijmans, 2017)	GCS WGS 1984	180W-180E, 90S-90N	30"
Annual Mean Temperature	Original bioclimatic variables provided by WorldClim.				
Mean Temperature of Warmest Quarter					
Mean Temperature of Coldest Quarter					
Annual Mean Precipitation					
Precipitation of Wettest Quarter					
Precipitation of Driest Quarter					
Seismic Hazard	-	Pagani, et al. (M. Pagani, J. Garcia-Pelaez, R. Gee, K. Johnson, V. Poggi, R. Styron, G. Weatherill, M. Simionato, D. Viganò, L. Danciu, 2018)	GCS WGS 1984	180W-180E, 65S-90N	5'
Two-band Enhanced Vegetation Index (EVI2)	Vegetation Index and Phenology Vegetation Indices, VIP30 v.004. EVI2 was computed as average of original yearly files for 1981-2014 period.	NASA (LP DAAC)	GCS Unknown datum based upon the Clarke 1866 ellipsoid	180W-180E, 90S-90N	3'
Evapotranspiration	Five-year averages for 2011-2015, calculated from original corresponding .nc files that include 12 bands for each month.	Teraclimate (Abatzoglou, Dobrowski, Parks, & Hegewisch, 2018)	GCS WGS 1984	180W-180E, 90S-90N	2.5'
Groundwater Recharge	Maps for January 2010, extracted from original .nc files of model input/output.	PCRGLOBWEB 2.0 (Sutanudjaja et al., 2018)	GCS WGS 1984	180W-180E, 90S-90N	5'
Water Storage Thickness					
Storage Capacity					
Note: As the final step, all maps were either cropped or extended with no-data values to match the extent of the Global Land Cover map.					

Table S2. Description of the 60 predictors, used in this study as predictors.

n	Predictor	Min	Max	Mean	STD	SHAP Score	Impact
1	GW Abstraction	0.0	3889.4	54.5	133.7	2.56	(+)
2	Precipitation Wettest Quarter	0.0	6637.0	318.8	298.4	1.58	(-)
3	Seismic Hazard	0.0	13.2	0.7	1.1	1.56	(+)
4	Annual Precipitation	0.0	9312.0	713.4	682.1	1.32	(-)
5	Organic Carbon Density	30.8	1179.7	198.5	87.4	1.32	(-)
6	Evapotranspiration	0.0	128.0	39.6	27.9	1.21	(-)
7	Precipitation Driest Quarter	0.0	1649.0	69.1	102.1	0.74	Mixed
8	GW Recharge	-0.1	0.6	0.0	0.0	0.60	(-)
9	Coarse Fragments Content	0.0	790.5	154.9	79.6	0.60	Mixed
10	Clay Content	9.7	846.5	260.9	84.9	0.50	(+)
11	EVI2	0.0	6559.8	2167.9	1173.3	0.38	(+)
12	Population	0.0	128122.7	28.4	155.1	0.31	(+)
13	Mean Temperature Warmest Quarter	-12.8	38.5	20.6	8.1	0.28	(+)
14	Water Storage Thickness	0.0	7155.7	85.1	248.9	0.28	(+)
15	Storage Capacity	0.0	0.2	0.1	0.0	0.27	Mixed
16	Soil Thickness	0.0	50.0	15.3	20.2	0.22	(+)
17	Slope	0.0	70.7	2.4	4.3	0.17	Mixed
18	Wetness Index	-1.0	19.3	6.0	1.8	0.16	(+)
19	Water Pressure	0.0	3.2	1.1	0.7	0.15	Mixed
20	Mean Temperature Coldest Quarter	-44.7	29.3	0.3	19.2	0.14	Mixed
21	Annual Mean Temperature	-25.3	31.4	10.6	13.4	0.13	Mixed
22	Land Cover	-	-	-	-	-	-
23	Lithology	-	-	-	-	-	-

Table S3. Statistics of the 23 predictors, as well as their importance and impact. "(+)", "(-)", and "Mixed" denotes whether a feature has a direct, inverse, or mixed relationship with subsidence rate, respectively.

Predictor	Pre-processing	Source	Projection	Extent	Resolution
Lithology	Original vector layers were rasterized and resampled to 30" resolution.	GLiM (Hartmann & Moosdorf, 2012)	World Eckert IV	180W-180E, 90S-90N	-
Land Cover	-	GLC2000 ('Joint Research Centre, Global Land Cover 2000 (2003)';, n.d.)	GCS WGS 1984	180W-180E, 56S-90N	30"
Climate		Kottek, et al. (Kottek, Grieser, Beck, Rudolf, & Rubel, 2006)		180W-180E, 90S-90N	5'
Biomes		Dinerstein, et al. (Dinerstein et al., 2017)		180W-180E, 90S-83.6N	-
Administrative Boundaries (includes 195 countries)		World Administrative Boundaries ('World Administrative Boundaries', n.d.)		180W-180E, 58.5S-83.6N	-
Regions		Ellis, et al. (Ellis & Ramankutty, 2008)		180W-180E, 55.8S-83.1N	5'
Anthropogenic Biomes	Anthropogenic biomes map was used to				
Urban Areas and Dense Settlements					

	extract two classes, namely “Urban Land” and “Dense Settlements”. These classes were combined for further zonal analysis.				
Population in 2020 using “Middle of the road” scenario	Shared Socioeconomic Pathways (Gao, 2020)		180W-180E, 55.8S-83.6N	30"	
Note: All files were converted to shapefiles, to use ArcGIS Zonal Statistics tool for further zonal analysis.					

Table S4. Global datasets used for defining the boundaries when calculating zonal statistics.

Administrative Boundaries (includes 195 countries)	Subsidence Extent (km ²)	Affected Population	Extent of Affected Urban Areas (km ²)	Mean Rate (mm/y)	Max Rate (mm/y)
Abyei	0	0	0	1.5	2.6
Afghanistan	127201	14633752	49	5.5	209.5
Aksai Chin	2981	5019	0	2.8	64.6
Albania	119	8549	0	1.5	14.3
Algeria	18812	4061885	475	1.6	169.3
American Samoa	0	0	0	0.0	0.0
Andorra	0	0	0	1.5	1.5
Angola	367	9154	0	1.5	9.6
Anguilla	0	0	0	0.0	0.0
Antigua & Barbuda	0	0	0	1.5	1.5
Argentina	76492	2473572	681	1.8	181.2
Armenia	2760	197865	36	2.6	71.6
Aruba	0	0	0	0.0	0.0
Arunachal Pradesh	5319	335737	12	2.2	22.4
Australia	20385	190136	75	1.5	52.1
Austria	85	21528	28	1.5	13.0
Azerbaijan	22380	3298012	166	5.6	131.6
Azores Islands	0	0	0	0.0	0.0
Bahamas	0	0	0	1.5	1.5
Bahrain	0	0	0	1.5	1.5
Bangladesh	88208	137151082	8484	9.3	57.3
Barbados	0	0	0	0.0	0.0
Belarus	6671	211745	55	1.8	34.0
Belgium	14	2416	1	1.5	7.4
Belize	373	6137	0	1.7	23.6
Benin	0	0	0	1.5	4.4
Bermuda	0	0	0	0.0	0.0

Bhutan	1973	144986	24	2.0	22.0
Bolivia	7926	117696	0	1.5	54.2
Bosnia & Herzegovina	30	3294	0	1.5	11.3
Botswana	128	178	0	1.5	9.5
Bouvet Island	0	0	0	0.0	0.0
Brazil	76796	2619451	529	1.5	32.2
British Indian Ocean Territory	0	0	0	0.0	0.0
British Virgin Islands	0	0	0	0.0	0.0
Brunei Darussalam	555	137132	50	3.3	30.6
Bulgaria	17	569	0	1.5	14.7
Burkina Faso	0	0	0	1.5	2.6
Burundi	304	162183	85	1.6	27.9
Cambodia	274	288437	36	1.7	8.8
Cameroon	3462	124321	1	1.5	21.1
Canada	304	71211	43	1.5	24.4
Cape Verde	0	0	0	0.0	0.0
Cayman Islands	0	0	0	0.0	0.0
Central African Republic	30	1160	0	1.5	15.5
Chad	318	8474	0	1.5	12.1
Chile	7319	2575732	298	1.6	130.4
China	1043460	368301538	68181	3.4	183.7
Christmas Island	0	0	0	0.0	0.0
Cocos (Keeling) Islands	0	0	0	0.0	0.0
Colombia	233787	21613906	996	4.9	43.4
Comoros	0	0	0	1.5	1.5
Congo	7184	42585	0	1.7	25.0
Cook Islands	0	0	0	0.0	0.0
Costa Rica	32918	4231936	285	12.6	68.6
Cote d'Ivoire	72	10025	0	1.4	14.8
Croatia	863	66065	0	1.6	19.3
Cuba	14032	1984871	248	2.8	50.2
Cyprus	76	10468	4	1.6	36.7
Czech Republic	6	3327	5	1.5	9.2
Democratic People's Republic of Korea	14	4266	1	1.5	7.3
Democratic Republic of the Congo	32114	2210070	218	1.6	30.0
Denmark	439	16596	3	1.5	21.5
Djibouti	108	54122	0	1.5	17.1
Dominica	0	0	0	1.5	1.5
Dominican Republic	8545	3175782	268	3.4	63.5
Ecuador	52175	3049387	161	4.8	66.0
Egypt	189	201061	43	1.5	80.5

El Salvador	5860	3069330	688	4.8	52.0
Equatorial Guinea	4028	187252	0	2.5	20.1
Eritrea	193	7915	0	1.5	12.4
Estonia	8	1164	0	1.5	12.7
Ethiopia	8255	2454823	213	1.5	57.8
Falkland Islands (Malvinas)	0	0	0	1.5	1.5
Faroe Islands	0	0	0	1.5	1.5
Fiji	0	0	0	1.5	1.5
Finland	9	375	0	1.5	6.8
France	602	103205	36	1.5	49.8
French Guiana	102	749	0	1.5	9.3
French Polynesia	0	0	0	0.0	0.0
French Southern and Antarctic Territories	0	0	0	0.0	0.0
Gabon	3372	104347	0	1.6	14.2
Gambia	0	0	0	1.5	2.8
Gaza Strip	6	44455	3	1.7	5.6
Georgia	7245	769863	265	3.0	32.9
Germany	346	29135	9	1.5	25.2
Ghana	133	46877	16	1.5	16.3
Gibraltar	0	0	0	0.0	0.0
Glorioso Islands	0	0	0	0.0	0.0
Greece	1167	138340	10	1.6	27.8
Greenland	0	0	0	0.0	0.0
Grenada	0	0	0	0.0	0.0
Guadeloupe	0	0	0	1.5	1.5
Guam	0	0	0	0.0	0.0
Guantanamo	0	0	0	1.5	1.5
Guatemala	13519	3474914	207	2.9	98.1
Guernsey	0	0	0	1.5	1.5
Guinea	113	80747	0	1.5	9.7
Guinea-Bissau	0	0	0	1.5	3.6
Guyana	319	15589	0	1.5	16.1
Haiti	2168	1184633	215	2.6	93.6
Hala'ib Triangle	5	14	0	1.5	9.8
Heard Island and McDonald Islands	0	0	0	0.0	0.0
Holy See	0	0	0	0.0	0.0
Honduras	4314	1253996	130	1.9	53.6
Hong Kong	0	0	0	1.5	1.5
Hungary	1126	95030	51	1.7	15.0
Iceland	0	0	0	1.5	1.5
Ilemi Triangle	0	0	0	1.5	1.5

India	670812	633080461	42987	3.8	82.4
Indonesia	843653	213435134	42556	11.3	50.8
Iran	791207	45882362	2306	15.5	238.3
Iraq	1680	115404	5	1.5	22.2
Ireland	0	0	0	1.5	1.5
Isle of Man	0	0	0	1.5	1.5
Israel	85	221885	34	1.5	10.5
Italy	14288	4257646	1109	2.0	89.2
Jamaica	5268	1943142	557	9.6	34.7
Jammu-Kashmir	6440	2141337	1099	2.0	58.0
Japan	4127	1275185	418	1.6	38.6
Jarvis Island	0	0	0	0.0	0.0
Jersey	0	0	0	1.5	1.5
Jordan	6	4699	0	1.5	7.7
Kazakhstan	66574	1420513	208	1.9	135.7
Kenya	3032	2630314	507	1.5	32.1
Kiribati	0	0	0	0.0	0.0
Kuril Islands	0	0	0	1.5	1.5
Kuwait	0	0	0	1.5	1.6
Kyrgyzstan	15458	1231715	108	2.9	156.3
Lao People's Democratic Republic	3051	297788	119	1.7	13.9
Latvia	0	0	0	1.5	5.2
Lebanon	250	26177	1	1.8	12.0
Lesotho	0	0	0	1.5	1.5
Liberia	1427	292578	18	1.8	23.4
Libyan Arab Jamahiriya	10484	2336441	36	1.5	95.9
Liechtenstein	4	1333	0	1.6	7.6
Lithuania	386	5367	0	1.5	17.4
Luxembourg	0	0	0	1.5	1.5
Macao	0	0	0	0.0	0.0
Madagascar	6594	1097722	34	1.6	17.8
Madeira Islands	0	0	0	0.0	0.0
Malawi	1122	526522	24	1.6	32.3
Malaysia	141738	21157329	3441	9.1	40.1
Maldives	0	0	0	0.0	0.0
Mali	310	32688	0	1.5	13.6
Malta	0	0	0	0.0	0.0
Marshall Islands	0	0	0	0.0	0.0
Martinique	0	0	0	0.0	0.0
Ma'tan al-Sarra	0	0	0	1.5	1.5
Mauritania	1823	205636	16	1.5	24.7

Mauritius	0	0	0	0.0	0.0
Mayotte	0	0	0	0.0	0.0
Mexico	66684	22061581	3149	2.0	321.5
Micronesia (Federated States of)	0	0	0	0.0	0.0
Midway Is.	0	0	0	0.0	0.0
Moldova, Republic of	458	38236	12	1.6	32.5
Monaco	0	0	0	1.5	1.5
Mongolia	15167	89317	0	1.6	119.8
Montenegro	1	48	0	1.5	6.3
Montserrat	0	0	0	1.5	1.5
Morocco	20387	4030740	384	2.2	176.9
Mozambique	2461	140074	2	1.5	18.8
Myanmar	87595	19703685	2022	2.8	73.7
Namibia	180	10274	0	1.5	10.9
Nauru	0	0	0	0.0	0.0
Nepal	11965	10087723	390	2.4	38.6
Netherlands	1	84	0	1.5	5.1
Netherlands Antilles	0	0	0	0.0	0.0
New Caledonia	212	5019	1	1.6	17.8
New Zealand	0	0	0	1.5	3.9
Nicaragua	5147	889255	43	2.0	48.0
Niger	14	2086	0	1.5	5.9
Nigeria	6316	5523014	1359	1.5	15.9
Niue	0	0	0	0.0	0.0
Norfolk Island	0	0	0	0.0	0.0
Northern Mariana Islands	0	0	0	0.0	0.0
Norway	410	14817	5	1.5	22.7
Oman	7925	850714	60	1.8	133.2
Pakistan	374172	145305722	7252	10.6	186.1
Palau	0	0	0	0.0	0.0
Panama	23460	1670384	223	6.1	30.2
Papua New Guinea	114366	2252952	48	5.6	37.7
Paracel Islands	0	0	0	0.0	0.0
Paraguay	4282	201242	55	1.6	33.9
Peru	39963	4151031	355	1.9	153.3
Philippines	205366	82218302	16771	19.3	52.1
Pitcairn Island	0	0	0	0.0	0.0
Poland	254	22121	11	1.5	11.4
Portugal	162	53139	7	1.5	13.8
Puerto Rico	1801	763083	357	4.1	26.9
Qatar	0	0	0	1.5	1.5

Republic of Korea	48	24278	1	1.5	10.3
Reunion	0	0	0	0.0	0.0
Romania	286	17777	0	1.5	28.5
Russian Federation	47415	2053021	720	1.5	98.4
Rwanda	157	105799	53	1.5	25.4
Saint Kitts and Nevis	0	0	0	0.0	0.0
Saint Lucia	0	0	0	0.0	0.0
Saint Vincent and the Grenadines	0	0	0	0.0	0.0
Samoa	0	0	0	0.0	0.0
San Marino	0	0	0	1.5	1.5
Sao Tome and Principe	0	0	0	0.0	0.0
Saudi Arabia	1725	161394	59	1.5	45.7
Senegal	19	1985	0	1.5	10.6
Serbia	57	6056	0	1.5	13.1
Seychelles	0	0	0	0.0	0.0
Sierra Leone	2766	430580	7	1.9	19.7
Singapore	89	959776	89	5.2	18.3
Slovakia	47	5630	0	1.5	12.6
Slovenia	94	15426	0	1.5	11.7
Solomon Islands	0	0	0	1.5	1.5
Somalia	7	4108	0	1.5	16.0
South Africa	701	133566	7	1.5	53.0
South Georgia & the South Sandwich Islands	0	0	0	0.0	0.0
South Sudan	23	352	0	1.5	5.8
Spain	24844	4505798	460	2.1	162.9
Spratly Islands	0	0	0	0.0	0.0
Sri Lanka	385	279222	45	1.6	8.0
Sudan	1550	150652	19	1.5	26.6
Suriname	7	7	0	1.5	10.7
Svalbard and Jan Mayen Islands	0	0	0	0.0	0.0
Swaziland	29	2575	0	1.5	6.3
Sweden	245	7064	0	1.5	19.5
Switzerland	3	1290	0	1.5	7.1
Syrian Arab Republic	18186	4611953	199	2.6	79.5
Taiwan	3537	4323801	1378	2.7	26.9
Tajikistan	14791	2389152	469	4.3	186.7
Thailand	59026	16079060	1822	3.0	39.6
The former Yugoslav Republic of Macedonia	6	327	0	1.5	10.3
Timor-Leste	711	112827	5	2.0	20.3
Togo	81	90825	4	1.5	12.3

Tokelau	0	0	0	0.0	0.0
Tonga	0	0	0	0.0	0.0
Trinidad and Tobago	1675	560976	215	7.2	31.5
Tunisia	14387	2159465	144	3.2	204.0
Turkey	63332	9238822	1531	2.5	113.2
Turkmenistan	140587	2327548	186	8.6	196.2
Turks and Caicos Islands	0	0	0	0.0	0.0
Tuvalu	0	0	0	0.0	0.0
U.K. of Great Britain and Northern Ireland	1	0	0	1.5	5.5
Uganda	2064	792304	101	1.6	28.5
Ukraine	12652	486747	116	1.7	34.8
United Arab Emirates	28368	7989648	93	9.7	117.7
United Republic of Tanzania	17634	3608362	302	1.7	33.8
United States of America	88366	2416193	1310	1.7	181.0
United States Virgin Islands	0	0	0	0.0	0.0
Uruguay	67	223	0	1.5	10.8
Uzbekistan	130662	18211196	1232	10.9	171.4
Vanuatu	1515	36886	13	4.8	34.4
Venezuela	53645	8314131	954	2.3	69.7
Vietnam	35299	36360000	8301	2.7	35.9
West Bank	0	0	0	1.5	2.9
Western Sahara	0	0	0	1.5	1.9
Yemen	4077	2652502	20	1.6	108.9
Zambia	4607	179753	0	1.6	13.3
Zimbabwe	285	15541	0	1.5	11.2
	TOTAL			MEAN	MAX
	6.3 M	1.9 B	231 K	1.9	321.5

Table S5. Statistics of the total subsidence area at the administrative boundary level. (>5 mm/y rate cutoff).

Region	Cumulative Subsidence Extent				Mean rate (mm/y)	Max rate (mm/y)
	>5mm/y	>15mm/y	>25mm/y	>50mm/y		
Australia and New Zealand	20385	2752	696	0	1.5	52.1
Caribbean	33489	6269	955	60	3.3	93.6
Central America	152274	59769	16152	2071	2.4	321.5
Central Asia	368073	199085	127194	44105	3.8	196.2
Eastern Africa	46825	3617	180	1	1.5	57.8
Eastern Asia	1081091	366627	185962	47560	3.0	183.7

Eastern Europe	68932	8067	2468	443	1.5	98.4
Melanesia	116093	69886	11620	0	5.2	37.7
Micronesia	0	0	0	0	0.0	0.0
Middle Africa	50897	1164	34	0	1.5	30.0
Northern Africa	65814	14201	6313	1990	1.6	204.0
Northern America	88670	27541	17409	7080	1.6	181.0
Northern Europe	1499	37	0	0	1.5	22.7
Polynesia	0	0	0	0	0.0	0.0
South America	552881	207159	64197	2664	1.9	181.2
South-Eastern Asia	1377359	922825	498614	67	7.7	73.7
Southern Africa	1038	65	8	1	1.5	53.0
Southern Asia	2065924	911846	504784	138632	7.9	238.3
Southern Europe	41632	5801	1272	96	1.8	162.9
Western Africa	13075	86	0	0	1.5	24.7
Western Asia	158102	46026	16987	1834	2.0	133.2
Western Europe	1055	17	10	0	1.5	49.8
	TOTAL				MEAN	MAX
	6.3 M	2.8 M	1.5 M	247 K	2.5	321.5

Table S6. Statistics of the subsidence affected areas at the region level.

Data Set S1. Global dataset of subsidence rates.

Data Set S2. Zonal statistics and feature importance.

Data Set S3. Raster subsidence map.

References

- Abatzoglou, J. T., Dobrowski, S. Z., Parks, S. A., & Hegewisch, K. C. (2018). TerraClimate, a high-resolution global dataset of monthly climate and climatic water balance from 1958–2015. *Scientific Data*, 5. doi:10.1038/sdata.2017.191
- Abdollahi, S., Pourghasemi, H. R., Ghanbarian, G. A., & Safaeian, R. (2019). Prioritization of effective factors in the occurrence of land subsidence and its susceptibility mapping using an SVM model and their different kernel functions. *Bulletin of Engineering Geology and the Environment*, 78(6), 4017–4034. doi:10.1007/s10064-018-1403-6
- Arabameri, A., Chandra Pal, S., Rezaie, F., Chakrabortty, R., Chowdhuri, I., Blaschke, T., & Thi Ngo, P. T. (2021). Comparison of multi-criteria and artificial intelligence models

- for land-subsidence susceptibility zonation. *Journal of Environmental Management*, 284. doi:10.1016/j.jenvman.2021.112067
- Arabameri, A., Santosh, M., Rezaie, F., Saha, S., Coastache, R., Roy, J., ... moayedi, H. (2022). Application of novel ensemble models and k-fold CV approaches for Land subsidence susceptibility modelling. *Stochastic Environmental Research and Risk Assessment*, 36(1), 201–223. doi:10.1007/s00477-021-02036-7
- Auvinet, G., Méndez, E., & Juárez, M. (2017). Recent information on Mexico City subsidence. In *ICSMGE 2017 - 19th International Conference on Soil Mechanics and Geotechnical Engineering* (Vol. 2017-Sept, pp. 3295–3298).
- Azarakhsh, Z., Azadbakht, M., & Matkan, A. (2022). Estimation, modeling, and prediction of land subsidence using Sentinel-1 time series in Tehran-Shahriar plain: A machine learning-based investigation. *Remote Sensing Applications: Society and Environment*, 25. doi:10.1016/j.rsase.2021.100691
- Bagheri-Gavkosh, M., Hosseini, S. M., Ataie-Ashtiani, B., Sohani, Y., Ebrahimian, H., Morovat, F., & Ashrafi, S. (2021). Land subsidence: A global challenge. *Science of the Total Environment*, 778. doi:10.1016/j.scitotenv.2021.146193
- Bekaert, D. P. S., Hamlington, B. D., Buzzanga, B., & Jones, C. E. (2017). Spaceborne Synthetic Aperture Radar Survey of Subsidence in Hampton Roads, Virginia (USA). *Scientific Reports*, 7(1). doi:10.1038/s41598-017-15309-5
- Blewitt, G., Kreemer, C., Hammond, W. C., & Gazeaux, J. (2016). MIDAS robust trend estimator for accurate GPS station velocities without step detection. *Journal of Geophysical Research: Solid Earth*, 121(3). doi:10.1002/2015JB012552
- Chaussard, E., Amelung, F., & Abidin, H. Z. (2012). Sinking cities in Indonesia: space-geodetic evidence of the rates and spatial distribution of land subsidence. *Proc. 'Fringe 2011 Workshop', Frascati, Italy, 19–23 September 2011 (ESA SP-697, January 2012)*, 2011(September 2011), 19–23. Retrieved from https://earth.esa.int/documents/10174/1573054/Sinking_cities_Indonesia_space-geodetic_evidence_rates_spatial_distribution_land_subsidence.pdf
- Chen, M., Tomás, R., Li, Z., Motagh, M., Li, T., Hu, L., ... Gong, X. (2016). Imaging land subsidence induced by groundwater extraction in Beijing (China) using satellite radar interferometry. *Remote Sensing*, 8(6). doi:10.3390/rs8060468
- Chen, Q., Liu, G., Ding, X., Hu, J. C., Yuan, L., Zhong, P., & Omura, M. (2010). Tight integration of GPS observations and persistent scatterer InSAR for detecting vertical ground motion in Hong Kong. *International Journal of Applied Earth Observation and Geoinformation*, 12(6), 477–486. doi:10.1016/j.jag.2010.05.002
- Cigna, F., & Tapete, D. (2021). Present-day land subsidence rates, surface faulting hazard and risk in Mexico City with 2014–2020 Sentinel-1 IW InSAR. *Remote Sensing of Environment*, 253. doi:10.1016/j.rse.2020.112161
- Del Soldato, M., Farolfi, G., Rosi, A., Raspini, F., & Casagli, N. (2018). Subsidence evolution of the Firenze-Prato-Pistoia plain (Central Italy) combining PSI and GNSS data. *Remote Sensing*, 10(7). doi:10.3390/rs10071146
- Dinerstein, E., Olson, D., Joshi, A., Vynne, C., Burgess, N. D., Wikramanayake, E., ... Saleem, M. (2017). An Ecoregion-Based Approach to Protecting Half the Terrestrial Realm. *BioScience*. doi:10.1093/biosci/bix014

- Dong, S., Samsonov, S., Yin, H., Ye, S., & Cao, Y. (2014). Time-series analysis of subsidence associated with rapid urbanization in Shanghai, China measured with SBAS InSAR method. *Environmental Earth Sciences*, 72(3), 677–691. doi:10.1007/s12665-013-2990-y
- Du, Y., Feng, G., Liu, L., Fu, H., Peng, X., & Wen, D. (2020). Understanding land subsidence along the coastal areas of Guangdong, China, by analyzing multi-track MTInSAR data. *Remote Sensing*, 12(2). doi:10.3390/rs12020299
- Ebrahimi, H., Feizizadeh, B., Salmani, S., & Azadi, H. (2020). A comparative study of land subsidence susceptibility mapping of Tasuj plane, Iran, using boosted regression tree, random forest and classification and regression tree methods. *Environmental Earth Sciences*, 79(10). doi:10.1007/s12665-020-08953-0
- El Kamali, M., Papoutsis, I., Loupasakis, C., Abuelgasim, A., Omari, K., & Kontoes, C. (2021). Monitoring of land surface subsidence using persistent scatterer interferometry techniques and ground truth data in arid and semi-arid regions, the case of Remah, UAE. *Science of the Total Environment*, 776. doi:10.1016/j.scitotenv.2021.145946
- Ellis, E. C., & Ramankutty, N. (2008). Putting people in the map: Anthropogenic biomes of the world. *Frontiers in Ecology and the Environment*. doi:10.1890/070062
- Elmahdy, S. I., Mohamed, M. M., Ali, T. A., Abdalla, J. E. D., & Abouleish, M. (2022). Land subsidence and sinkholes susceptibility mapping and analysis using random forest and frequency ratio models in Al Ain, UAE. *Geocarto International*, 37(1), 315–331. doi:10.1080/10106049.2020.1716398
- Erban, L. E., Gorelick, S. M., & Zebker, H. A. (2014). Groundwater extraction, land subsidence, and sea-level rise in the Mekong Delta, Vietnam. *Environmental Research Letters*, 9(8). doi:10.1088/1748-9326/9/8/084010
- Fick, S. E., & Hijmans, R. J. (2017). WorldClim 2: new 1-km spatial resolution climate surfaces for global land areas. *International Journal of Climatology*, 37(12), 4302–4315. doi:10.1002/joc.5086
- Gao, J. (2020). Global 1-km downscaled population base year and projection grids based on the shared socioeconomic pathways, Revision 01. Retrieved from <https://doi.org/10.7927/q7z9-9r69>
- Gebremichael, E., Sultan, M., Becker, R., El Bastawesy, M., Cherif, O., & Emil, M. (2018). Assessing Land Deformation and Sea Encroachment in the Nile Delta: A Radar Interferometric and Inundation Modeling Approach. *Journal of Geophysical Research: Solid Earth*, 123(4), 3208–3224. doi:10.1002/2017JB015084
- Haghshenas Haghghi, M., & Motagh, M. (2019). Ground surface response to continuous compaction of aquifer system in Tehran, Iran: Results from a long-term multi-sensor InSAR analysis. *Remote Sensing of Environment*, 221, 534–550. doi:10.1016/j.rse.2018.11.003
- Hartmann, J., & Moosdorf, N. (2012). The new global lithological map database GLiM: A representation of rock properties at the Earth surface. *Geochemistry, Geophysics, Geosystems*, 13(12). doi:10.1029/2012GC004370
- Heleno, S. I. N., Oliveira, L. G. S., Henriques, M. J., Falcão, A. P., Lima, J. N. P., Cooksley, G., ... Fonseca, J. F. B. D. (2011). Persistent Scatterers Interferometry detects and measures ground subsidence in Lisbon. *Remote Sensing of Environment*, 115(8),

- 2152–2167. doi:10.1016/j.rse.2011.04.021
- Hengl, T., De Jesus, J. M., Heuvelink, G. B. M., Gonzalez, M. R., Kilibarda, M., Blagotić, A., ... Kempen, B. (2017). SoilGrids250m: Global gridded soil information based on machine learning. *PLoS ONE*, 12(2). doi:10.1371/journal.pone.0169748
- Herrera-García, G., Ezquerro, P., Tomas, R., Béjar-Pizarro, M., López-Vinielles, J., Rossi, M., ... Ye, S. (2021). Mapping the global threat of land subsidence. *Science*, 371(6524), 34–36. doi:10.1126/science.abb8549
- Heywood, C. E., Galloway, D. L., & Stork, S. V. (2002). *Ground Displacements Caused by Aquifer- System Water-Level Variations Observed Using Interferometric Synthetic Aperture Radar near Albuquerque , New Mexico Ground Displacements Caused by Aquifer- System Water-Level Variations Observed Using Interferometri. U.S. GEOLOGICAL SURVEY Water-Resources Water-Resources Investigations Report 02-4235.*
- Ho Tong Minh, D., Van Trung, L., & Le Toan, T. (2015). Mapping ground subsidence phenomena in Ho Chi Minh City through the radar interferometry technique using ALOS PALSAR data. *Remote Sensing*, 7(7), 8543–8562. doi:10.3390/rs70708543
- Hung, W. C., Hwang, C., Chen, Y. A., Zhang, L., Chen, K. H., Wei, S. H., ... Lin, S. H. (2018). Land subsidence in Chiayi, Taiwan, from compaction well, leveling and ALOS/PALSAR: Aquaculture-induced relative sea level rise. *Remote Sensing*, 10(1). doi:10.3390/rs10010040
- Hwang, C., Yang, Y., Kao, R., Han, J., Shum, C. K., Galloway, D. L., ... Li, F. (2016). Time-varying land subsidence detected by radar altimetry: California, Taiwan and north China. *Scientific Reports*, 6. doi:10.1038/srep28160
- Ilia, I., Loupasakis, C., & Tsangaratos, P. (2018). Land subsidence phenomena investigated by spatiotemporal analysis of groundwater resources, remote sensing techniques, and random forest method: the case of Western Thessaly, Greece. *Environmental Monitoring and Assessment*, 190(11). doi:10.1007/s10661-018-6992-9
- Joint Research Centre, Global Land Cover 2000 (2003); (n.d.). Retrieved from <https://forobs.jrc.ec.europa.eu/products/glc2000/glc2000.php>
- Kakar, N., Kakar, D. M., & Barrech, S. (2020). *Land subsidence caused by groundwater exploitation in Quetta and surrounding region, Pakistan*. In *Proceedings of the International Association of Hydrological Sciences* (Vol. 382, pp. 595–607). doi:10.5194/piahs-382-595-2020
- Khorrami, M., Abrishami, S., Maghsoudi, Y., Alizadeh, B., & Perissin, D. (2020). Extreme subsidence in a populated city (Mashhad) detected by PSInSAR considering groundwater withdrawal and geotechnical properties. *Scientific Reports*, 10(1). doi:10.1038/s41598-020-67989-1
- Kottek, M., Grieser, J., Beck, C., Rudolf, B., & Rubel, F. (2006). World map of the Köppen-Geiger climate classification updated. *Meteorologische Zeitschrift*, 15(3), 259–263. doi:10.1127/0941-2948/2006/0130
- Li, J., Wang, S., Michel, C., & Russell, H. A. J. (2020). Surface deformation observed by InSAR shows connections with water storage change in Southern Ontario. *Journal of Hydrology: Regional Studies*, 27. doi:10.1016/j.ejrh.2019.100661
- Li, X., Yan, L., Lu, L., Huang, G., Zhao, Z., & Lu, Z. (2021). Adjacent-track insar processing

- for large-scale land subsidence monitoring in the hebei plain. *Remote Sensing*, 13(4), 1–23. doi:10.3390/rs13040795
- Lundberg, S. M., & Lee, S. I. (2017). A unified approach to interpreting model predictions. In *Advances in Neural Information Processing Systems* (Vol. 2017-Decem, pp. 4766–4775).
- M. Pagani, J. Garcia-Pelaez, R. Gee, K. Johnson, V. Poggi, R. Styron, G. Weatherill, M. Simionato, D. Vigano, L. Danciu, D. M. (2018). Global Earthquake Model Global Seismic Hazard. *Dec 05, 2018*, 475.
- Malik, K., Kumar, D., Perissin, D., & Pradhan, B. (2022). Estimation of ground subsidence of New Delhi, India using PS-InSAR technique and Multi-sensor Radar data. *Advances in Space Research*, 69(4), 1863–1882. doi:10.1016/j.asr.2021.08.032
- Marthews, T. R., Dadson, S. J., Lehner, B., Abele, S., & Gedney, N. (2015). High-resolution global topographic index values for use in large-scale hydrological modelling. *Hydrology and Earth System Sciences*, 19(1), 91–104. doi:10.5194/hess-19-91-2015
- Mekonnen, M. M., & Hoekstra, A. Y. (2011). *National water footprint accounts: the green, blue and grey water footprint of production and consumption, Value of Water Research Report Series No. 50. Hydrology and Earth System Sciences Discussions* (Vol. 8).
- Mohammady, M., Pourghasemi, H. R., & Amiri, M. (2019). Land subsidence susceptibility assessment using random forest machine learning algorithm. *Environmental Earth Sciences*, 78(16). doi:10.1007/s12665-019-8518-3
- Motagh, M., Shamshiri, R., Haghshenas Haghghi, M., Wetzel, H. U., Akbari, B., Nahavandchi, H., ... Arabi, S. (2017). Quantifying groundwater exploitation induced subsidence in the Rafsanjan plain, southeastern Iran, using InSAR time-series and in situ measurements. *Engineering Geology*, 218, 134–151. doi:10.1016/j.enggeo.2017.01.011
- Najafi, Z., Pourghasemi, H. R., Ghanbarian, G., & Fallah Shamsi, S. R. (2020). Land-subsidence susceptibility zonation using remote sensing, GIS, and probability models in a Google Earth Engine platform. *Environmental Earth Sciences*, 79(21). doi:10.1007/s12665-020-09238-2
- Ng, A. H. M., Ge, L., Li, X., Abidin, H. Z., Andreas, H., & Zhang, K. (2012). Mapping land subsidence in Jakarta, Indonesia using persistent scatterer interferometry (PSI) technique with ALOS PALSAR. *International Journal of Applied Earth Observation and Geoinformation*, 18(1), 232–242. doi:10.1016/j.jag.2012.01.018
- Othman, A., & Abotalib, A. Z. (2019). Land subsidence triggered by groundwater withdrawal under hyper-arid conditions: case study from Central Saudi Arabia. *Environmental Earth Sciences*, 78(7). doi:10.1007/s12665-019-8254-8
- Othman, A., Sultan, M., Becker, R., Alsefry, S., Alharbi, T., Gebremichael, E., ... Abdelmohsen, K. (2018). Use of Geophysical and Remote Sensing Data for Assessment of Aquifer Depletion and Related Land Deformation. *Surveys in Geophysics*. doi:10.1007/s10712-017-9458-7
- Parker, A. L., Filmer, M. S., & Featherstone, W. E. (2017). First results from sentinel-1A InSAR over Australia: Application to the Perth Basin. *Remote Sensing*, 9(3). doi:10.3390/rs9030299

- Pelletier, J. D., Broxton, P. D., Hazenberg, P., Zeng, X., Troch, P. A., Niu, G. Y., ... Gochis, D. (2016). A gridded global data set of soil, intact regolith, and sedimentary deposit thicknesses for regional and global land surface modeling. *Journal of Advances in Modeling Earth Systems*, 8(1), 41–65. doi:10.1002/2015MS000526
- Pourghasemi, H. R., & Mohseni Saravi, M. (2019). Land-Subsidence Spatial Modeling Using the Random Forest Data-Mining Technique. In *Spatial Modeling in GIS and R for Earth and Environmental Sciences* (pp. 147–159). doi:10.1016/b978-0-12-815226-3.00006-5
- Rafiei Sardooi, E., Pourghasemi, H. R., Azareh, A., Soleimani Sardoo, F., & Clague, J. J. (2021). Comparison of statistical and machine learning approaches in land subsidence modelling. *Geocarto International*. doi:10.1080/10106049.2021.1933211
- Rahmati, O., Falah, F., Naghibi, S. A., Biggs, T., Soltani, M., Deo, R. C., ... Tien Bui, D. (2019). Land subsidence modelling using tree-based machine learning algorithms. *Science of the Total Environment*, 672, 239–252. doi:10.1016/j.scitotenv.2019.03.496
- Raspini, F., Loupasakis, C., Rozos, D., & Moretti, S. (2013). Advanced interpretation of land subsidence by validating multi-interferometric SAR data: The case study of the Anthemountas basin (Northern Greece). *Natural Hazards and Earth System Sciences*, 13(10), 2425–2440. doi:10.5194/nhess-13-2425-2013
- Raspini, Federico, Cigna, F., & Moretti, S. (2012). Multi-temporal mapping of land subsidence at basin scale exploiting persistent scatterer interferometry: Case study of Gioia Tauro plain (Italy). *Journal of Maps*, 8(4), 514–524. doi:10.1080/17445647.2012.743440
- Rohatgi, A. (n.d.). WebPlotDigitizer. Retrieved from <https://automeris.io/WebPlotDigitizer>
- Salehi Moteahd, F., Hafezi Moghaddas, N., Lashkaripour, G. R., & Dehghani, M. (2019). Geological parameters affected land subsidence in Mashhad plain, north-east of Iran. *Environmental Earth Sciences*, 78(14). doi:10.1007/s12665-019-8413-y
- Sekkeravani, M. A., Bazrafshan, O., Pourghasemi, H. R., & Holisaz, A. (2022). Spatial modeling of land subsidence using machine learning models and statistical methods. *Environmental Science and Pollution Research*, 29(19), 28866–28883. doi:10.1007/s11356-021-18037-6
- Smith, R. G., & Majumdar, S. (2020). Groundwater Storage Loss Associated With Land Subsidence in Western United States Mapped Using Machine Learning. *Water Resources Research*, 56(7). doi:10.1029/2019WR026621
- Subsidence in San Joaquin Valley. (n.d.). Retrieved from <https://mavensnotebook.com/2013/11/22/in-her-own-words-usgs-hydrologist-discusses-subsidence-in-the-central-valley/>
- Sutanudjaja, E. H., Van Beek, R., Wanders, N., Wada, Y., Bosmans, J. H. C., Drost, N., ... Bierkens, M. F. P. (2018). PCR-GLOBWB 2: A 5 arcmin global hydrological and water resources model. *Geoscientific Model Development*, 11(6), 2429–2453. doi:10.5194/gmd-11-2429-2018
- TRE Altamira Dataset. (2015). Retrieved from <https://data.cnra.ca.gov/dataset/tre-altamira-insar-subsidence/resource/2535a9b9-ed25-4b19-9734-4b1409e3fdce>
- USGS. (1996). GTOPO30: Global 30 Arc Second Elevation Data Set. *Online: Http://Www1.Gsi.Go.Jp/Geowww/Globalmap-Gsi/Gtopo30/Gtopo30.Html* (Accessed

02/05/2012).

- van der Horst, T., Rutten, M. M., van de Giesen, N. C., & Hanssen, R. F. (2018). Monitoring land subsidence in Yangon, Myanmar using Sentinel-1 persistent scatterer interferometry and assessment of driving mechanisms. *Remote Sensing of Environment*, 217, 101–110. doi:10.1016/j.rse.2018.08.004
- Wen, T., Tiewang, W., Arabameri, A., Asadi Nalivan, O., Pal, S. C., Saha, A., & Costache, R. (2022). Land-subsidence susceptibility mapping: assessment of an adaptive neuro-fuzzy inference system–genetic algorithm hybrid model. *Geocarto International*. doi:10.1080/10106049.2022.2066198
- World Administrative Boundaries. (n.d.). Retrieved from <https://public.opendatasoft.com/explore/dataset/world-administrative-boundaries/export/?dataChart=eyJxdWVyaWVzIjpbeJjb25maWciOnsiZGF0YXNlIdCl6IndvcmxkLWFkbWluaXN0cmF0aXZILWJvdW5kYXJpZXMiLCJvcHRpb25zIjp7fX0slmNoYXJ0cyl6W3siYWxpZ25Nb250aCI6dHJ1ZSwidHlwZSI6I>
- Yu, J., Wang, G., Kearns, T. J., & Yang, L. (2014). Is there deep-seated subsidence in the houston-galveston area? *International Journal of Geophysics*, 2014. doi:10.1155/2014/942834
- Zamanirad, M., Sarraf, A., Sedghi, H., Saremi, A., & Rezaee, P. (2020). Modeling the Influence of Groundwater Exploitation on Land Subsidence Susceptibility Using Machine Learning Algorithms. *Natural Resources Research*, 29(2), 1127–1141. doi:10.1007/s11053-019-09490-9